ARTICLE

The nature of cell division forces in epithelial monolayers

Vivek K. Gupta[1] ⓘ, Sungmin Nam[1,2,3], Donghyun Yim[4] ⓘ, Jaclyn Camuglia[5], Judy Lisette Martin[6], Erin Nicole Sanders[6] ⓘ, Lucy Erin O'Brien[6] ⓘ, Adam C. Martin[5] ⓘ, Taeyoon Kim[4], and Ovijit Chaudhuri[1] ⓘ

Epithelial cells undergo striking morphological changes during division to ensure proper segregation of genetic and cytoplasmic materials. These morphological changes occur despite dividing cells being mechanically restricted by neighboring cells, indicating the need for extracellular force generation. Beyond driving cell division itself, forces associated with division have been implicated in tissue-scale processes, including development, tissue growth, migration, and epidermal stratification. While forces generated by mitotic rounding are well understood, forces generated after rounding remain unknown. Here, we identify two distinct stages of division force generation that follow rounding: (1) Protrusive forces along the division axis that drive division elongation, and (2) outward forces that facilitate postdivision spreading. Cytokinetic ring contraction of the dividing cell, but not activity of neighboring cells, generates extracellular forces that propel division elongation and contribute to chromosome segregation. Forces from division elongation are observed in epithelia across many model organisms. Thus, division elongation forces represent a universal mechanism that powers cell division in confining epithelia.

Introduction

Epithelia are tightly packed sheets of cells that line the surfaces of organs and cavities. Cell division within epithelial tissues occurs continuously during development, homeostasis, and regeneration, and is critical for expanding tissues or replenishing cells lost due to extrusion, apoptosis, or injury (Guillot and Lecuit, 2013). Dividing cells are surrounded by adjacent cells and the underlying basement membrane, creating a confining microenvironment (Fig. 1 a). As cell division occurs typically within the plane of the monolayer, the extreme morphological changes that are required for cell division to progress normally must be accompanied by extracellular forces, or division forces. Beyond driving cell division itself, division forces have been implicated in contributing to distinct processes, including development, cell rearrangements, cell migration, epidermal stratification, and growth (Krndija et al., 2019; da Silva and Vincent, 2007; Firmino et al., 2016; Parker et al., 2017; Mammoto et al., 2012; Kondo and Hayashi, 2013; Doostmohammadi et al., 2015; Miroshnikova et al., 2018).

While division forces are critical for successful division completion, as well as various tissue-scale processes, the nature and origins of these forces remain unclear, beyond the well-studied process of mitotic rounding. In mitotic rounding, which

occurs before metaphase, the dividing cell transitions to a rounded morphology by generating forces through a combination of actomyosin contractility and hydrostatic pressure (Sorce et al., 2015; Lancaster et al., 2013; Cattin et al., 2015; Maddox and Burridge, 2003; Rosa et al., 2015; Stewart et al., 2011); however, after mitotic rounding, the dividing cell continues to undergo morphological changes as it elongates along the division axis and is cleaved at its center by a cytokinetic ring. Both of these processes are critical for proper segregation of chromosomes and other cytoplasmic materials and are required for successful completion of division (Nam and Chaudhuri, 2018). Furthermore, the resulting rounded daughter cells then undergo spreading as they reintegrate into the monolayer to maintain proper barrier function (Fig. 1 b). Although mitotic rounding in epithelia has been studied extensively, the extracellular forces generated after mitotic rounding remain largely unexplored.

Results

Three stages of force generation associated with division

Here, we investigated the forces accompanying cell division in epithelial monolayers. Through the entire course of division,
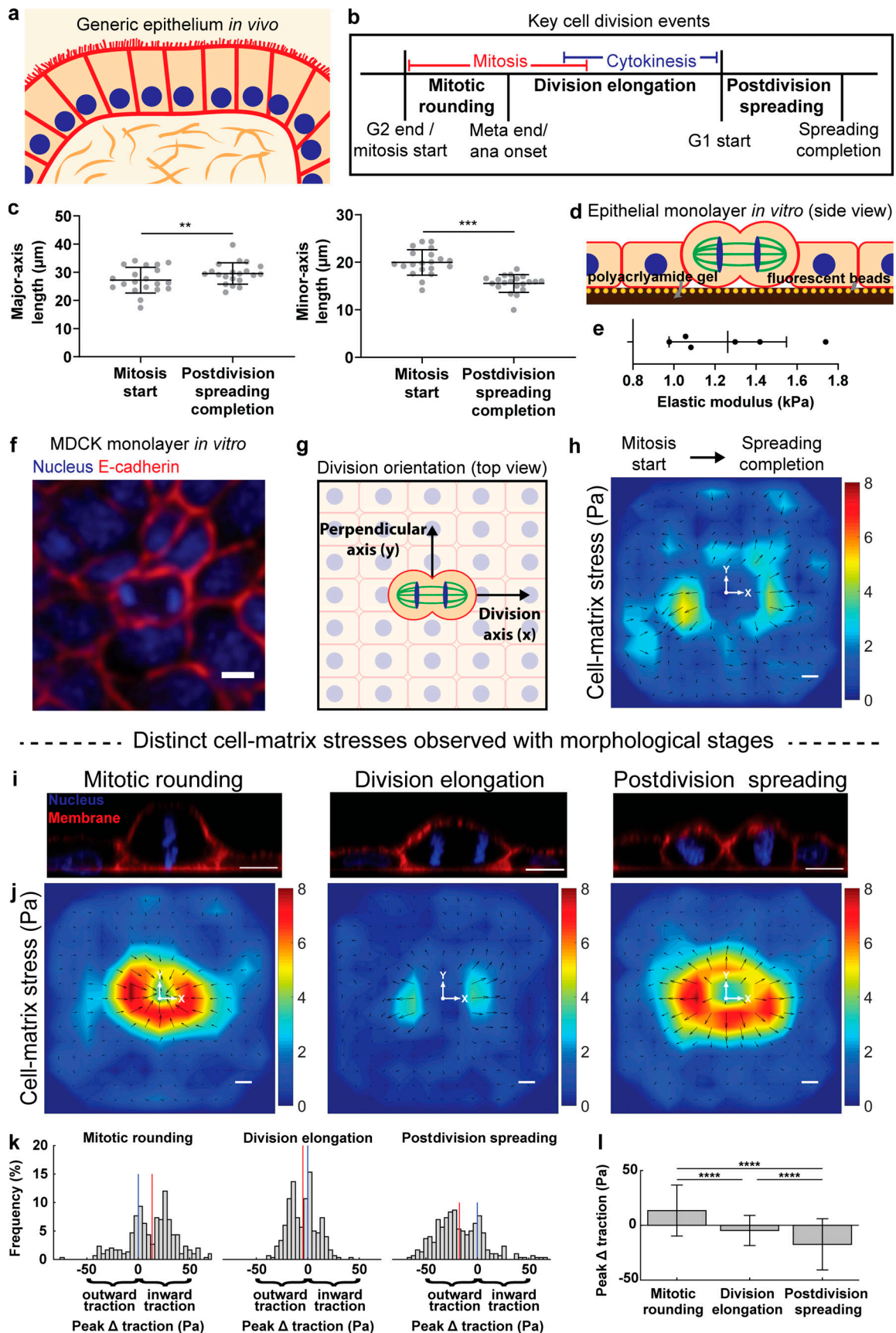
Figure 1. **Cell division within epithelial monolayers is associated with three distinct stages of cell–matrix and cell–cell stress: Mitotic rounding, division elongation, and postdivision spreading. (a)** Schematic of a generic epithelium in vivo (side view). **(b)** Timeline of mitotic rounding, division

elongation, and postdivision spreading with respect to cell cycle and division progression. **(c)** Net change in length of parent and daughter cell pair from mitosis start to postdivision spreading completion along the major and minor axes. $n = 20$; mean ± SD; paired two-sample t test. **(d)** Experimental setup (side view) of MDCK epithelial monolayer grown on polyacrylamide gel substrate with embedded fluorescent beads. **(e)** Elastic moduli measurements of polyacrylamide gel. **(f)** Image of cell division event within MDCK epithelial monolayer (top view). **(g)** Schematic of division axis (x) and perpendicular axis (y) orientations for the traction force microscopy and monolayer stress microscopy heat maps. **(h)** Net average change in cell–matrix stress from start of mitosis to postdivision spreading completion. $n = 300$. **(i)** Side-view images of the three morphological processes occurring during cell division: Mitotic rounding, division elongation, and postdivision spreading. **(j–l)** Average change in cell–matrix stress (j) and their distribution (k and l) during the three stages associated with division. Outward (pointing away from the origin) traction stresses were defined to be negative, and inward (pointing toward the origin) traction stresses were defined to be positive. Vertical red lines indicate means; blue line at 0 Pa; edge bins contain exceeding values as well; $n = 300$; mean ± SD; Tukey's multiple comparison test. Scale bars, 10 μm. **, $P < 0.01$; ***, $P < 0.001$; ****, $P < 0.0001$.

starting with a spread parent cell at mitosis onset and ending with two daughter cells after completing postdivision spreading, we found an increase in length along the major axis and a decrease in length along the minor axis in MDCK epithelial monolayers (Fig. 1c). This redistribution of mass suggests that net forces should be generated through the entire course of division. To investigate, MDCK monolayers were grown on soft (~1 kPa) polyacrylamide gels coated with type I collagen and embedded with fluorescent beads (Fig. 1, d–f). Cell division events were identified and traction force (TFM) and monolayer stress microscopy (MSM) were used to measure changes in cell–matrix and cell–cell stresses during cell division, respectively, along the division and perpendicular axes (Fig. 1 g; Trepat et al., 2009; Tambe et al., 2011). Because measured cell–matrix and cell–cell stresses are calculated based on forces applied by dynamic cell–matrix adhesions, many division events (>100) were averaged and aligned to isolate forces solely associated with cell division (Rossen et al., 2014). Through the entire course of cell division, encompassing the time period over which a spread parent cell becomes two spread daughter cells, we found there to be a net outward stress (Fig. 1 h; and Fig. S1, a–i).

Based on morphological changes and measured stresses, cell division was categorized into three distinct chronological stages: mitotic rounding, division elongation, and postdivision spreading (Fig. 1, b and i). On average, net inward stresses develop during mitotic rounding of cells in relatively flat MDCK monolayers (Fig. 1, i–l); however, mitotic rounding can be separated into two phases based on cell–matrix stresses, with net inward stresses generated during the initial phase and net outward stresses occurring during the 6-min period before metaphase (Fig. S1, j and k). Previously, more cuboidal or columnar epithelia have been associated only with net outward stresses during mitotic rounding, likely due to the different geometry of cells (Sorce et al., 2015). During division elongation, encompassing elongation of the interpolar spindle at anaphase onset through cytokinesis completion, outward stresses develop, primarily along the division axis. Finally, outward stresses develop in all directions as the daughter cells spread back onto the underlying substrate (Fig. 1, i–l). Cell–cell stresses are consistent with cell–matrix stresses, with inward cell–matrix stresses associated with tensile cell–cell stresses and outward cell–matrix stresses associated with compressive cell–cell stresses (Fig. S1, a–i). Measured stress values for division elongation and postdivision spreading were comparable to those of mitotic rounding. We note that TFM and MSM likely underestimate the true value of division stresses, because cell division occurs primarily

at the center plane of the monolayer, while these techniques rely on measurements of substrate deformation that are made at the basal monolayer plane. Indeed, previous measurements of mitotic rounding forces with atomic force microscopy have reported stresses on the order of ~500 Pa and forces on the order of 50–100 Nn (Cattin et al., 2015; Stewart et al., 2011). Stresses during division elongation were significantly more anisotropic and skewed along the division axis, with the average stress along the perpendicular axis less than 25% of the average stress along the division axis compared with mitotic rounding and postdivision spreading, in which perpendicular axis stresses were ~75% of division axis stresses. Comparable results were found for MCF10A epithelial monolayers (Fig. S2) and MDCK monolayers at varying densities (Fig. S3, a–h). Cells did not exhibit the same cell–matrix stress trends before mitotic rounding or after postdivision spreading, confirming that these observed stresses are not part of a greater trend within cell cycle progression (Fig. S3, i and j). Furthermore, neighboring cells either along the division axis or perpendicular axis did not exhibit the same cell–matrix stress trends, confirming that stresses observed are not part of a general trend within the epithelial monolayer (Fig. S3, k–p). Thus, these analyses identified three distinct stages of extracellular force generation—mitotic rounding, division elongation, and postdivision spreading—associated with cell division in epithelial monolayers.

The dividing cell drives division elongation
Next, we considered the origins of force generation in division elongation and postdivision spreading, the two stages of extracellular force generation revealed in this study. While previous studies have not linked postdivision spreading of epithelial cells to outward force generation within monolayers, they do indicate that postdivision spreading is similar to general cell spreading, which is powered through the formation of cell–matrix adhesions and actin polymerization (Cramer and Mitchison, 1995; Dix et al., 2018). In contrast to the well-understood mechanisms underlying spreading, forces generated by division elongation have only been studied in the context of single, isolated cancer cells embedded within inert alginate hydrogels, a context lacking neighboring cells and cell–matrix adhesions (Nam and Chaudhuri, 2018).

Thus, we investigated the mechanisms underlying division elongation in epithelial monolayers. We reasoned that there were three possible sources of the forces underlying elongation: (1) Pulling forces from adjacent cells that cause elongation of the dividing cell; (2) movement of adjacent cells away from the

dividing cells, which would open up space for division elongation to occur as the cells de-adhere from the substrate; or (3) the dividing cell itself pushes outward to generate space for elongation (Fig. 2 a). Cell-cell adhesions within epithelial monolayers are expected to be under tension due to actomyosin contractility (Borghi et al., 2012), making it possible that tension transmitted across cell–cell adhesions along the division axis pull the dividing cell apart. In this case, we would expect cells to be dividing against cell edges (single cells), rather than against cell vertices (cell pairs), for tension to be transmitted symmetrically along the division axis (Fig. 2 b); however, we found cells to divide against both cell edges and vertices (Fig. 2 c). Furthermore, the nuclei of adjacent cells were randomly distributed with respect to the dividing cell (Fig. 2, d and e), indicating that the division axis orientation is independent of the arrangement of neighboring cells, making it unlikely that neighboring cells coordinate to drive division elongation. To further test this idea, the role of E-cadherin, a cell–cell adhesion protein known to transmit tension between cells to the actin cytoskeleton, was examined by using cells overexpressing a mutant E-cadherin with a truncated extracellular domain that cannot transmit forces between cells (Fig. 2, f–h; Borghi et al., 2012; Troxell et al., 2000). In mosaic monolayers (Fig. 2 i), division of truncated E-cadherin cells was accompanied by larger protrusive cell–matrix stresses compared with WT cells (Fig. 2, j and k). These data indicate that the intracellular domain of E-cadherin was not necessary for the protrusive stresses, though the increase in protrusive stresses with the truncated E-cadherin is surprising. Overall, these data establish that the forces of division elongation do not arise from neighboring cells pulling on the dividing cell.

We next considered the movement of cells adjacent to the dividing cell. Nuclei of adjacent cells were tracked as the dividing cell transitions from metaphase to cytokinesis completion. While motile, the neighboring nuclei were not consistently moving away from or toward the dividing cell (Fig. 3, a–c). Cell adhesions were examined as release of neighboring cell adhesions near the dividing cell could also create space for division elongation to occur. MDCK cells stably expressing vinculin::GFP, a marker for focal adhesions, were imaged during division (Fig. 3 d). Adhesions within a 50 × 30-μm area (longer dimension oriented along division axis) were identified, and similar numbers were found when at metaphase and cytokinesis completion (Fig. 3 e), suggesting that adjacent cells do not de-adhere from the substrate during division elongation. Although it is possible that some adhesions imaged originated from the dividing cell rather than neighboring cells, previous work has suggested that cells do not generally maintain mature focal adhesions during division (Dix et al., 2018). Taken together, these results support the conclusion that adjacent cells do not migrate away from dividing cells.

With the role of the neighboring cells in driving division elongation eliminated as a possibility, we directly investigated whether observed division forces originated from the dividing cell pushing outward against its neighbors. We imaged the cell membrane and nuclei of cells laying adjacent to the dividing cell along the division axis. As the dividing cell elongated, adjacent cells and their nuclei were deformed, exhibiting reduced cross-sectional areas at the center plane compared with that of perpendicular or neighboring cells (Fig. 4, a–f). Deformation of cells was only observed for cells along the division axis and synchronized with division elongation. Furthermore, the increased curvature (κ) of the neighboring cell edge along the division axis indicates the application of protrusive forces by the dividing cell to the cell edge (Fig. 4, g and h). Taken together, these results indicate that division elongation arises due to the dividing cell pushing outward.

We next examined how forces generated by the dividing cell during division elongation are transmitted to the underlying substrate. Although forces from the dividing cell push outward, the dividing cell is only tethered to the substrate via thin actin-based retraction fibers and integrins (Fink et al., 2011; Dix et al., 2018). Neighboring interphase cells, in contrast, are secured to the substrate through typical cell–matrix adhesions. Additionally, during division progression, neighboring cells are known to extend protrusions underneath the dividing cell (Uroz et al., 2018). Thus, it is likely that, as apical portions of neighboring cells are pushed outward, the underlying substrate is also pulled outward via cell–matrix adhesions of the neighboring cells, generating the observed cell–matrix stresses (Fig. 1, j–l). Mosaic imaging of actin at the basal plane confirmed that neighboring cells are adhered to the substrate underneath the dividing cell (Fig. 5 a), and this region overlaps with where outward substrate deformations during division elongation were typically measured (Fig. 5, b and c). In agreement with this, single cells dividing in isolation did not generate any consistent force pattern during division elongation, and generated outward forces during mitotic rounding and inward forces during postdivision spreading (Fig. 5, d and e). Although TFM and MSM are useful techniques for estimating monolayer forces in general, the different physical cell movements occurring across z-planes means computed stress values are likely underestimated due to neighboring cell deformation that occurs at the center plane but with forces being read at the basal plane. To get a more accurate estimate of force generation during division elongation, the finite element method was applied. The 3D deformation of adjacent cells was first measured (Fig. 5, f and g), and then, treating the adjacent cells as fully elastic objects, finite element method analysis was used to estimate adjacent cell deformation for varying levels of force application. Simulations showed that forces in the range of 300–500 nN most closely replicated deformations of the adjacent cell induced by dividing cells (Fig. 5, h and i), indicating that force values are much greater than those indicated by TFM and MSM (Fig. 1, j–l; and Fig. S1, a–i). Taken together, our results reveal that stresses generated by the dividing cell during elongation are transmitted to the substrate by adhesions of adjacent cells (Fig. 5 j).

Force generation mechanisms for division elongation
Next, we sought to determine how the dividing cell generates protrusive forces during division elongation. A previous study found that cancer cells embedded within inert hydrogels exert protrusive forces during the early parts of elongation using interpolar spindle elongation and during the later stages of
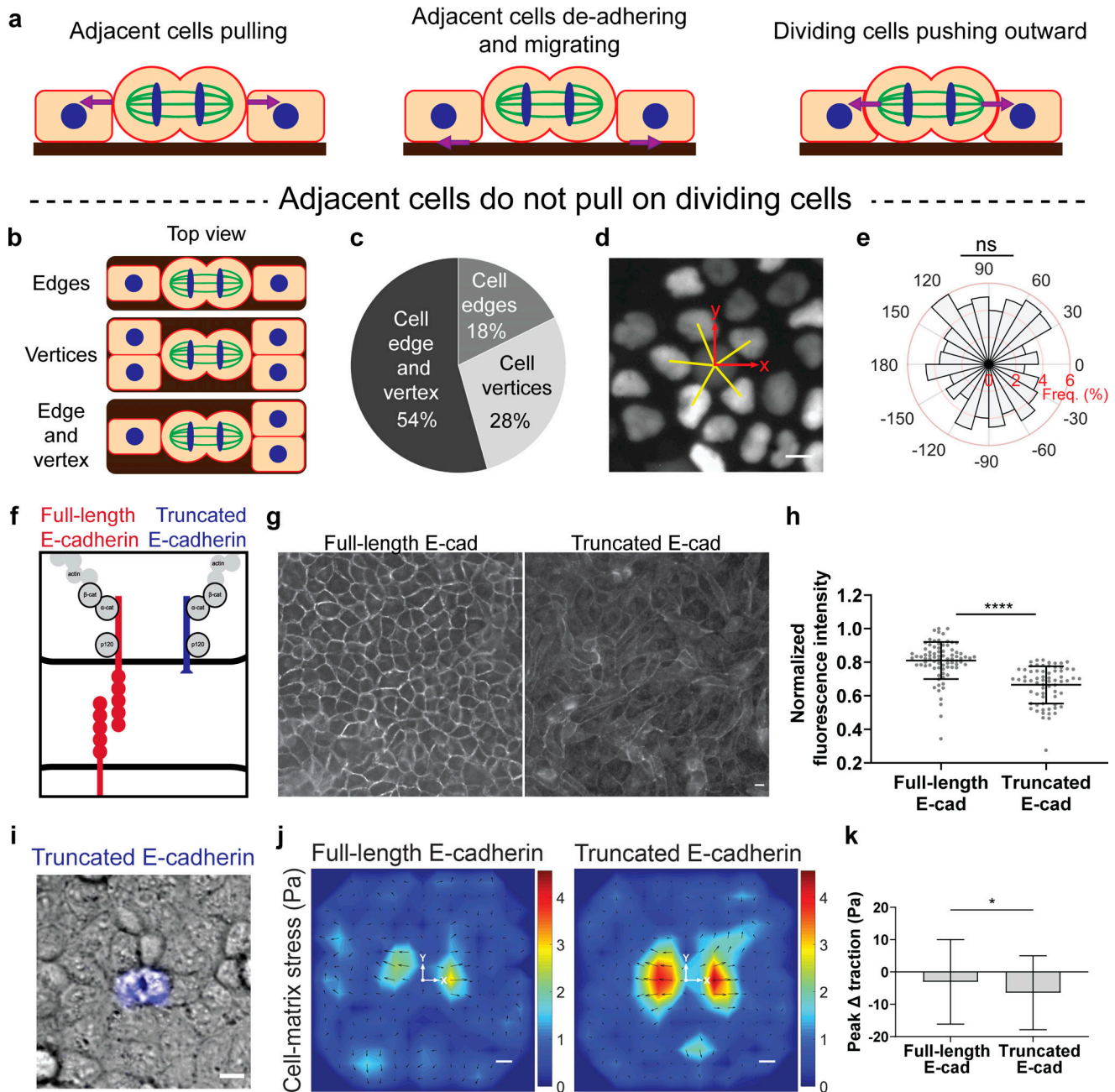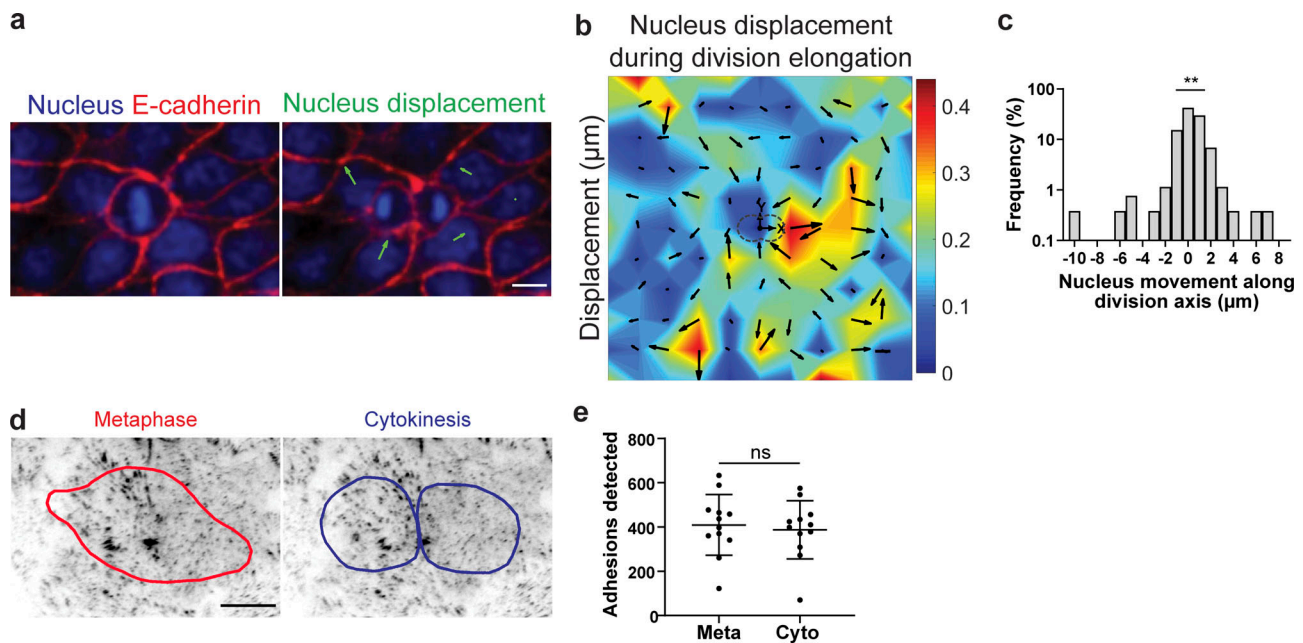
Figure 2. **Forces generated during division elongation do not originate from adjacent cells pulling on the dividing cell along the division axis. (a)** Side-view schematics displaying potential mechanisms that drive division elongation include adjacent cells pulling, adjacent cells migrating, or the dividing cell pushing outward. **(b and c)** Schematic showing top view of cells dividing against cell edges (single cells), cell vertices (cell pairs), or a cell edge and a vertex (b), and corresponding frequency distribution (c). n = 212. **(d)** Fluorescent image of nuclei neighboring a dividing cell, with yellow lines indicating angle between the dividing cell and neighboring cell's nuclei. **(e)** Distribution of angles between dividing and neighboring cell nuclei. n = 602 nuclei (from 152 dividing cells); χ² test against difference from uniform distribution. **(f)** Cartoon depicting structure of full-length and truncated E-cadherin protein (Hart et al., 2017). **(g and h)** MDCK cells with dominant expression of truncated E-cadherin exhibit reduced levels of extracellular E-cadherin. Representative images of fluorescent stain of extracellular E-cadherin for MDCK WT cells (full-length) and MDCK cells stably expressing truncated E-cadherin (g) and the fluorescent intensity quantification (h). n = 80 (full-length E-cadherin), n = 67 (truncated E-cadherin); mean ± SD; unpaired two-sample t test. **(i)** Image of mosaic monolayer with MDCK cell expressing E-cadherin with a truncated extracellular domain surrounded by WT MDCK cells. **(j and k)** Average change in cell–matrix stress during division elongation generated with WT and truncated E-cadherin cells. n = 116; mean ± SD; unpaired two-sample t test. Scale bars, 10 μm. *, P < 0.05; ****, P < 0.0001.

Figure 3. **Forces generated during division elongation do not originate from the movement of adjacent cells. (a)** Representative movement of nuclei adjacent to a dividing cell. **(b)** Average displacement of nuclei neighboring dividing cells. Dividing cell is centered on the heat map, with the division axis oriented along the horizontal (x) axis. n = 152. **(c)** Quantification of adjacent nuclei movement along the division axis, with positive numbers indicating movement away and negative numbers indicating movement toward the dividing cell. n = 261 adjacent nuclei (from 152 dividing cells); one-sample t test. **(d)** Reverse-contrast images of vinculin::GFP in MDCK cell at metaphase and cytokinesis completion. Image shows area (50 × 30 µm) used for detection of adhesions in one of the experiments. Outline of dividing cell is shown. **(e)** The number of detected adhesions at metaphase and cytokinesis. n = 12; mean ± SD; paired two-sample t test. Scale bars, 10 µm. **, $P < 0.01$.

elongation using cytokinetic ring contraction, which drives expansion along the division axis due to conservation of volume (Fig. 6 a; Nam and Chaudhuri, 2018). Consistent with the possibility of both of these mechanisms contributing, cells elongate and generate compressive stresses through the entire course of division elongation in epithelial monolayers (Fig. 6, b and c); therefore, we examined the contribution of these mechanisms to division elongation.

We first assessed the contribution of interpolar spindle elongation to protrusive force generation during division elongation. During the early parts of elongation, kinesin motor proteins, including kinesin-5, push cross-linked interpolar microtubules apart, and these forces can potentially be transmitted to the neighboring cells via astral microtubules (Fig. 6 a; Nam and Chaudhuri, 2018); however, interpolar spindle elongation was not correlated with cell elongation (Fig. 6, d and e). To inhibit interpolar spindle elongation, cells at prometaphase and onward (Fig. 6 f) were treated with BRD9876, which increases kinesin-5 binding (Chattopadhyay et al., 2015). Interpolar spindle elongation and cell elongation were reduced by similar amounts (Fig. 6, g and h). Kinesin-5 inhibition also decreased the tendency of dividing cells to deform adjacent cells (Fig. 6 i); however, treatment with S-trityl-L-cysteine, which reduces kinesin-5 binding (DeBonis et al., 2004; Skoufias et al., 2006), led to an increase in interpolar spindle elongation, but no change in cell elongation (Fig. 6, j and k). Next, laser ablation was used to sever the interpolar spindle of dividing cells during division elongation but before significant progression of cytokinetic ring

contraction. If the interpolar spindle elongation drives elongation, it should be under compression, and ablation of the structure should result in almost immediate retraction of the dividing cell's chromosomes and membrane. However, in contrast to previous work on single cancer cells dividing in alginate hydrogels, ablation resulted in chromosome and cell membrane retraction only in some cells (Fig. 6, l and m). 3D imaging confirmed that cell boundaries were not consistently retracting after interpolar spindle ablation (Fig. S4 a). Overall, our experiments show that interpolar spindle elongation might contribute to, but does not fully drive, division elongation and protrusive force generation in epithelial monolayers.

We next assessed the role of cytokinetic ring contraction in protrusive force generation during division elongation. As cytokinetic ring contraction occurs perpendicular to the division axis, perpendicular inward forces should lead to outward forces along the division axis if volume is conserved or nearly conserved (Fig. 6 a). The volume of dividing cells was measured before and after cytokinesis and was found to decrease by only 5% (Fig. 7 a). Using computational modeling, we evaluated how much a cell can be extended in the axial direction by a contractile force exerted on the equator of the cell (Fig. 7, b and c; and Fig. S4, b–f). Even with a 5% reduction in volume, decreasing ring sizes during cytokinesis were accompanied by 60% elongation along the division axis, suggesting a role for cytokinetic ring contraction in driving division elongation (Fig. 7 d). Reductions in volume on the order of 40% would be needed for cytokinetic ring contraction to not drive cell elongation (Fig. 7 e).
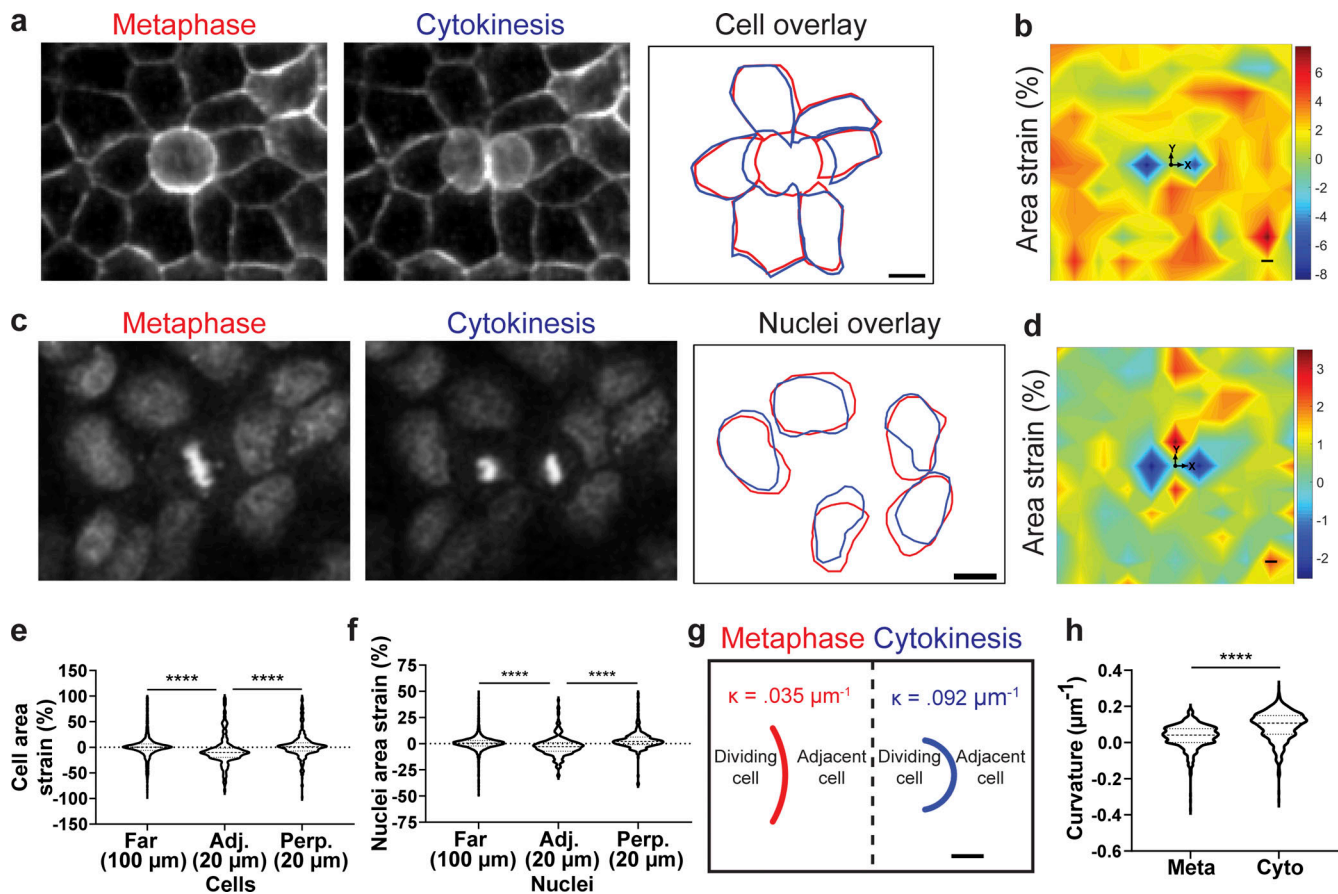
Figure 4. **Forces generated during division elongation originate from the dividing cell pushing outward against adjacent cells along the division axis.** **(a–d)** Images of adjacent cells (a) and nuclei (c) being deformed during division elongation, with corresponding averaged area strain heat maps (b and d). Dividing cell is centered on the heat map, with the division axis oriented along the horizontal (x) axis. $n = 200$ dividing cells (b), $n = 152$ dividing cells (d). **(e and f)** Quantification of cell (e) and nuclei (f) area strain between adjacent, perpendicular, and neighboring cells. $n = 12,371$ (far), $n = 369$ (adjacent), $n = 369$ (perpendicular; from 200 dividing cells; e); and $n = 8,621$ (far), $n = 258$ (adjacent), $n = 273$ (perpendicular; from 152 dividing cells; f); mean ± SD; Tukey's multiple comparison test. **(g and h)** Schematic displaying average change in curvature (κ) of an adjacent cell (g) and quantification (h) of curvatures at metaphase and cytokinesis completion. $n = 708$ adjacent cells (from 200 dividing cells); mean ± SD; paired two-sample t test. Scale bars, 10 µm. ****, $P < 0.0001$.

To directly test whether cytokinetic ring contraction is involved in cell elongation, cytokinesis was inhibited by adding blebbistatin (Straight et al., 2003). While inhibition of myosin could also impact cortical forces, only cells that had progressed to metaphase and were shortly beginning division elongation were considered in order to minimize the potential impact of cortical tension disruption on cell elongation (Fig. 6 f). Inhibition of cytokinetic ring contraction resulted in binucleate cells and almost completely abrogated cell elongation (60% reduction) and adjacent cell deformation during division elongation (Fig. 7, f and g). Importantly, inhibition of cytokinetic ring contraction also diminished chromosome segregation, highlighting the biological importance of the forces underlying division elongation for proper cell division (Fig. 7 h). Similar results were found for inhibition of polo-like kinase 1, which is essential for both anaphase B and cytokinesis progression (Fig. 7 i; Brennan et al., 2007). In addition, short interfering RNA (siRNA) knockdown of anillin (siANLN) within MCF10A cells resulted in dividing cells contracting their cytokinetic ring to varying degrees until cytokinesis failure (Fig. 7, j and k). Knockdown cells exhibited reduced cell elongation during division (Fig. 7 l). Furthermore,

within knockdown cells, cell elongation was correlated with the extent of maximum cytokinetic ring contraction (Fig. 7, m and n). Taken together, these results demonstrate that the forces for division elongation are generated by cytokinetic ring contraction.

Force generation by division elongation in vivo

After identifying division elongation as a direct force-generating stage in epithelial monolayers in vitro, we examined whether epithelial cells dividing within in vivo contexts also exert protrusive forces during elongation. Consistent deformation of cells adjacent to a dividing cell during elongation and an increase in curvature of the cell–cell boundary along the division axis would indicate protrusive force generation originating from the dividing cell. We first examined early *Drosophila* embryo cell division after the blastoderm stage, focusing on cells within mitotic domains 1 and 5 (Foe, 1989). Dividing cells consistently deformed adjacent cells at the center plane, which exhibited reduced cross-sectional areas and increased inward curvatures after division completion (Fig. 8, a–d). We note that, in contrast to MDCK and MCF10A epithelial monolayers grown in vitro,
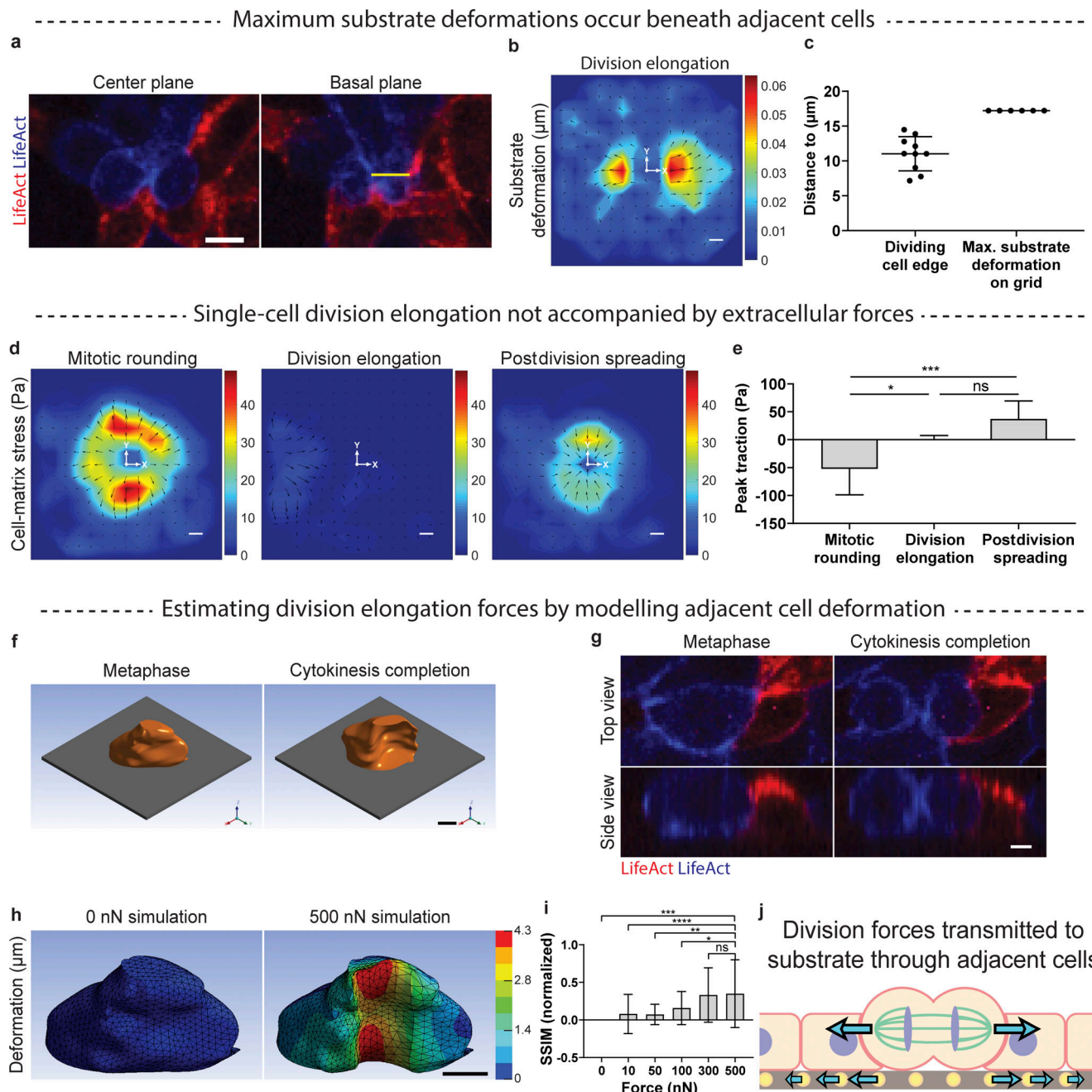
Figure 5. **Stress generated by dividing cell during elongation transmitted to substrate through adhesions of adjacent cells. (a)** Mosaic imaging of LifeAct displaying dividing cell in blue and adjacent cell in red at the center and basal planes. Yellow segment indicates distance from center of the dividing cell to dividing-adjacent cell boundary. **(b)** Average substrate deformations generated during division elongation. n = 300. Dividing cell is centered on the heat map, with the division axis oriented along the horizontal (x) axis. **(c)** Comparison between distance to dividing cell edge at the basal plane and distance to maximum substrate deformation from averaged substrate deformation heat map. n = 10 dividing cells (dividing cell edge), n = 6 maximum substrate deformation values obtained from averaged substrate deformation heat maps from 300 dividing cells; mean ± SD; scale bars = 10 μm. **(d and e)** Average change in cell–matrix stress (d) and their distribution (e) during the three stages associated with division, for single cells. Outward (pointing away from the origin) traction stresses were defined to be negative, and inward (pointing toward the origin) traction stresses were defined to be positive. n = 7; mean ± SD; Tukey's multiple comparison test; scale bars = 10 μm. **(f)** 3D rendering of adjacent cell surface at metaphase and cytokinesis completion, with red arrow indicating direction of dividing cell. Scale bar, 5 μm. **(g)** Top view and side view of LifeAct showing adjacent cell deformation during division elongation. Scale bar = 10 μm. **(h and i)** Deformation heat map of adjacent cell with 0 nN and 500 nN applied force (h), and normalized (against 0 nN) SSIM between experimental and simulated adjacent cell deformation for various force values (i). Scale bar, 5 μm. n = 32 z-slices (from three dividing cells); mean ± SD; Dunnett's multiple comparison test. **(j)** Schematic displaying outward substrate deformations due to pushing forces exerted by the dividing cell. *, $P < 0.05$; **, $P < 0.01$; ***, $P < 0.001$; ****, $P < 0.0001$.
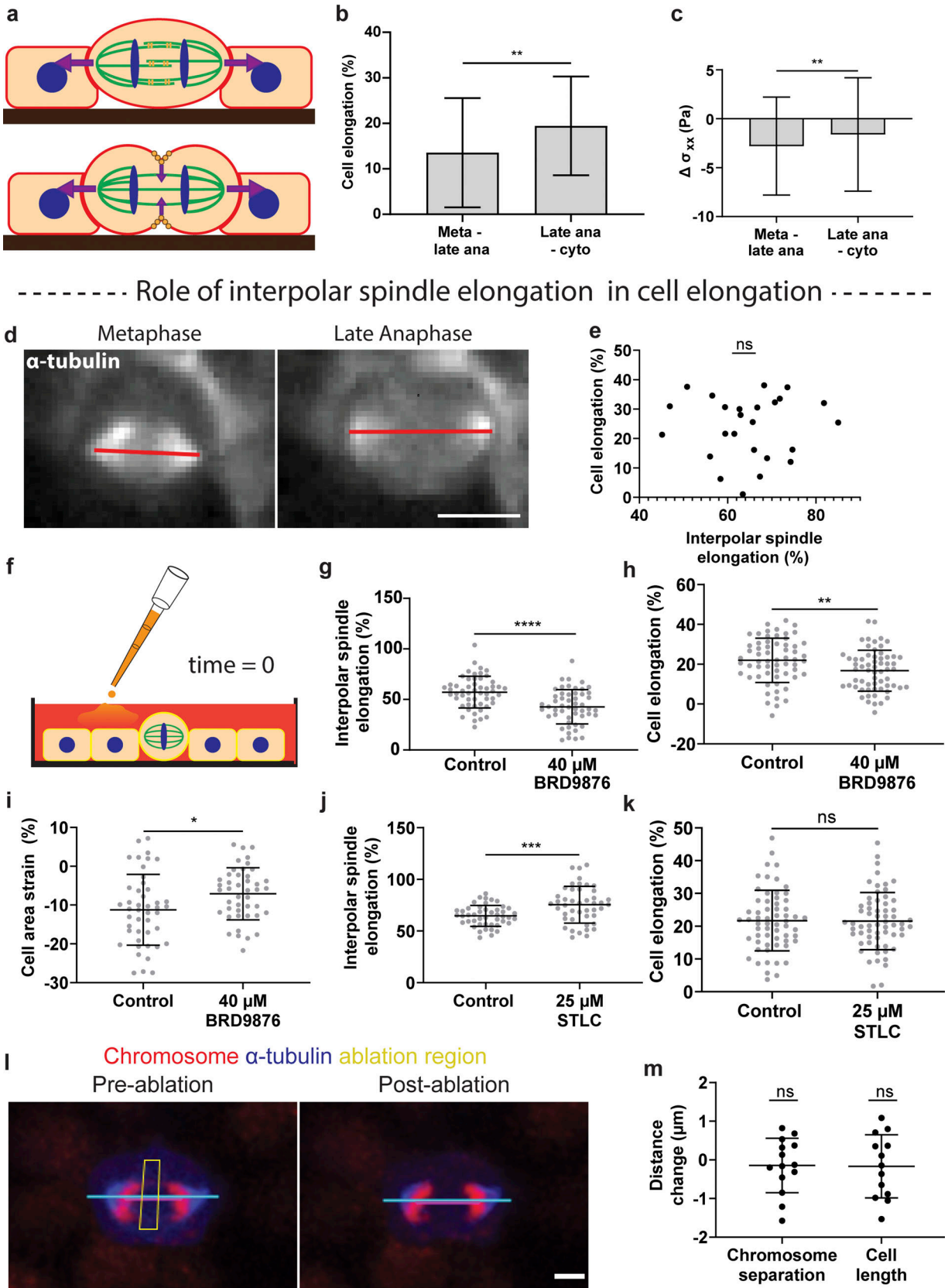
Figure 6. **Perturbation of interpolar spindle elongation impacts division elongation in only some cases. (a)** Side-view schematics illustrating that forces for division elongation can, in principle, be generated from interpolar spindle elongation and cytokinetic ring contraction. **(b and c)** Cell elongation (*n* = 94; b)

and change in cell–cell stress along the division axis ($\Delta \sigma_{xx}$; n = 300; c) during the early (metaphase to late anaphase) and late (late anaphase to cytokinesis completion) stages of division elongation. Mean ± SD; paired two-sample t test. **(d)** Quantification of interpolar spindle elongation between metaphase and late anaphase. Scale bar, 10 µm. **(e)** Lack of correlation between interpolar spindle and cell elongation. n = 25; Pearson's r. **(f)** Schematic of inhibition experiments in which inhibitor is added to cells at metaphase. **(g–i)** Interpolar spindle elongation (n = 53 control, n = 54 experimental; g), cell elongation (n = 61 control, n = 62 experimental; h), and adjacent cell area strain (n = 45 control, n = 44 experimental; i) quantification with and without kinesin-5 inhibition with BRD9876 treatment. Mean ± SD; unpaired two-sample t test. **(j and k)** Interpolar spindle elongation (n = 46 control, n = 45 experimental; j) and cell elongation (n = 61 control, n = 62 experimental; k) with and without kinesin-5 inhibition with S-trityl-L-cysteine (STLC) treatment. Mean ± SD; unpaired two-sample t test. **(l)** Laser ablation reveals the interpolar spindle does not consistently bear compression. Representative image of dividing MDCK cell before and after ablation of the interpolar spindle, with magenta line indicating chromosome separation and cyan line indicating cell length. Yellow box indicates ablation region. Scale bar, 5 µm. **(m)** Quantification of change in distance of chromosome separation (n = 14) and cell length (n = 13) before and after ablation. Negative values indicate chromosome or cell retraction. Mean ± SD; one-sample t test. *, P < 0.05; **, P < 0.01; ***, P < 0.001; ****, P < 0.0001.

Drosophila epithelia are columnar, not flat. Thus, it is possible that cells also generate outward forces during mitotic rounding, when cells transition from a columnar to spherical shape; however, perpendicular cells did not exhibit significant deformation, indicating that the deformation primarily arises from the asymmetric process of division elongation. Next, we examined division events in published literature and analyzed deformation of cell–cell junctions between dividing cells and neighboring cells across a variety of model organisms, including mouse, *Drosophila*, *Xenopus*, zebrafish, and *Caenorhabditis elegans* (Miroshnikova et al., 2018; Foe, 1989; Niwayama et al., 2019; Gudipaty et al., 2017; McKinley et al., 2018; Scarpa et al., 2018; Kieserman and Wallingford, 2009; Bai et al., 2020). Negative area strains in adjacent cells were observed in most cases (Fig. 8 e). Strikingly, positive changes in the curvature of cell–cell boundaries were observed in all instances, with no negative changes in curvature observed, an observation that can only be explained by protrusive force generation from the dividing cell (Fig. 8 f and Fig. S5). Interestingly, in the context of stem cells dividing within adult *Drosophila* intestines, the dividing cells recoiled shortly after completing division (Fig. 8, g and h). This suggests that the dividing stem cell was bearing compressive forces during division elongation, and upon division completion these forces are dissipated, which produces an inward motion of the daughter cells (Martin et al., 2018). Thus, the protrusive extracellular forces that drive division elongation appear to be ubiquitous across epithelia.

Discussion

Here, we show that cells dividing within epithelial monolayers generate distinct forces in three mitotic stages: Mitotic rounding, division elongation, and postdivision spreading. Inward stresses develop during mitotic rounding, outward stresses are generated along the division axis during elongation, and uniform outward stresses continue during postdivision spreading. Although the origins of force generation during mitotic rounding and their implications have been well studied, division elongation and postdivision spreading have been overlooked. Our results indicate that forces generated during division elongation originate from the dividing cell rather than neighboring cells, primarily due to cytokinetic ring contraction. Perturbation of interpolar spindle elongation impacted division elongation in only some cases, suggesting that the interpolar spindle only partially drives elongation. While it has been known that cells have the ability to generate large forces during cell spreading through the formation of robust adhesions and polymerization of branched actin networks, our work ties these forces to enabling reintegration of daughter cells into the monolayer. Beyond their role in driving division, division forces have been linked to tissue-scale biological processes, such as collective cell migration observed in intestinal crypts and villi (Parker et al., 2017; Krndija et al., 2019), cell rearrangements within chick embryos (Firmino et al., 2016), invagination within developing *Drosophila* embryos (Kondo and Hayashi, 2013; Ko et al., 2020), apical invagination during intestine villi formation (Freddo et al., 2016), and lumen growth (Hoijman et al., 2015). While previous work has typically attributed division forces to mitotic rounding, these processes are inherently anisotropic. Thus, division elongation could play a key, unappreciated role in contributing to or driving these important biological processes.

Materials and methods
Cell culture
Parental MDCK type II G cells and MDCK cells stably expressing the nuclear FUCCI cell cycle sensor (gift from Dr. William J. Nelson, Stanford University, Stanford, CA) or LifeAct::RFP (gift from Dr. Alexander Dunn, Stanford University, Stanford, CA) were grown in low-glucose DMEM (31600034; Thermo Fisher Scientific) supplemented with 10% FBS (SH30071.03; GE Healthcare), 1 g/liter sodium bicarbonate, and 100 U/ml penicillin-streptomycin (15140; Thermo Fisher Scientific). Growth media for MDCK cells stably expressing LifeAct::GFP (gift from Dr. Jens Möller, ETH Zurich, Zurich, Switzerland), E-cadherin:: DsRed, truncated E-cadherin (T151–), vinculin::GFP, or α-tubulin::GFP (gifts from Dr. William J. Nelson) were additionally supplemented with 250 µg/ml geneticin (10131027; Thermo Fisher Scientific). T151– cells were cultured with tetracycline-free FBS (SH30070.03T; GE Healthcare; Troxell et al., 2000). MCF10A WT and LifeAct::RFP mammary epithelial cells (CRL-10317; ATCC) were cultured in DMEM/F12 (11330057; Thermo Fisher Scientific) supplemented with 5% horse serum (16050122; Thermo Fisher Scientific), 20 ng/ml epidermal growth factor (AF-100-15; Peprotech), 0.5 µg/ml hydrocortisone (H0888; Sigma-Aldrich), 100 ng/ml cholera toxin (C8052; Sigma-Aldrich), 10 µg/ml insulin (91077C; Sigma-Aldrich), and 100 U/ml penicillin-streptomycin (Debnath et al., 2003).
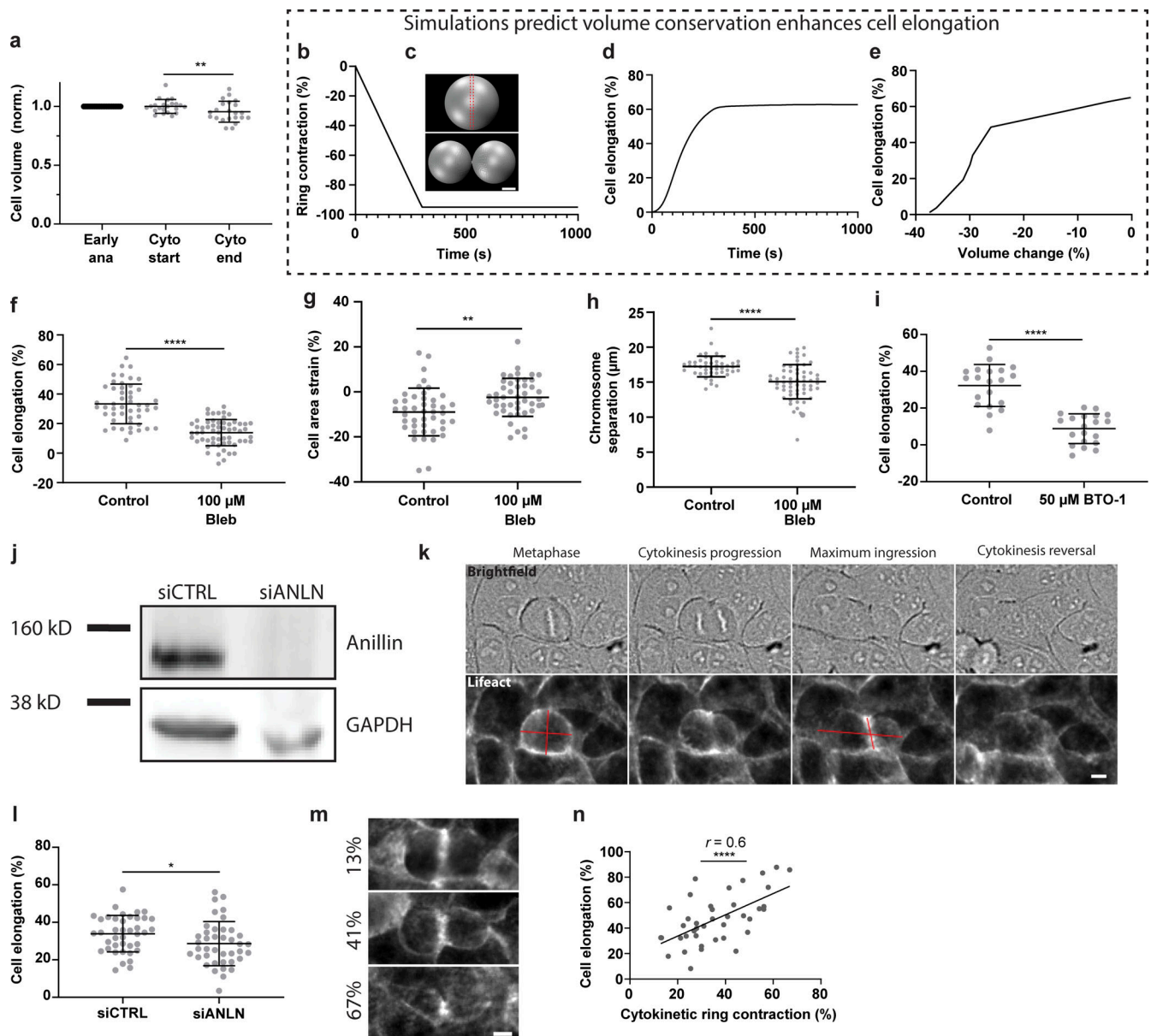
Figure 7. **Forces for division elongation are generated by cytokinetic ring contraction.** **(a)** Change in cell volume before and after cytokinesis. $n = 22$; mean ± SD; paired two-sample t test. **(b and c)** Simulation of cytokinetic ring contraction progression (b) and corresponding computational model (c). Scale bar, 5 μm. **(d)** Predicted cell elongation due to cytokinetic ring contraction for a 5% cell volume reduction. **(e)** Predicted cell elongation based on varying levels of cell volume reduction during division. **(f–h)** Cell elongation ($n = 49$ control, $n = 59$ experimental; f), adjacent cell area strain ($n = 44$ control, $n = 47$ experimental; g), and chromosome separation ($n = 47$ control, $n = 59$ experimental; h) with blebbistatin treatment. Mean ± SD; unpaired two-sample t tests. **(i)** Cell elongation with BTO-1 treatment. $n = 20$ control, $n = 20$ experimental; mean ± SD; unpaired two-sample t test. **(j)** Western blot indicating knockdown of anillin. Anillin and GAPDH were imaged at different intensities. $n = 1$. **(k)** Division time course displaying cell treated with siANLN fails to complete cytokinesis. Scale bar, 10 μm. **(l)** Cell elongation with siANLN or control (siCTRL) treatment. $n = 40$ control, $n = 40$ experimental; mean ± SD; unpaired two-sample t test. **(m)** Representative images of actin for siANLN cells at maximum cytokinetic ring contraction. Scale bar, 10 μm. **(n)** Correlation between maximum contractile ring contraction and cell elongation for siANLN cells. $n = 40$; Pearson's r. Scale bars, 10 μm. *, $P < 0.05$; **, $P < 0.01$; ****, $P < 0.0001$.

Polyacrylamide gel fabrication

Polyacrylamide gels were fabricated and functionalized with collagen-1 based on a mix of previously published protocols (Guo and Wang, 2011; Tse and Engler, 2010; Trepat et al., 2009; Plotnikov et al., 2014; Aratyn-Schaus et al., 2010; Przybyla et al., 2016). Glass-bottom dishes with a 20-mm bottom diameter were cleaned by incubation with 1 M NaOH for 30 min. The glass surface was activated to ensure covalent bonding with the polyacrylamide gel by incubating in a 950:50:3 solution of 95% ethanol, glacial acetic acid, and 3-(trimethoxysilyl)propyl methacrylate (M6514; Sigma-Aldrich), respectively, for 5 min. Dishes were rinsed with ethanol and dried with heat. A donut-shaped spacer was made from removable double-sided tape by punching holes with 12- and 18-mm-diameter hammer punches. The spacer was placed on the glass bottom. Top coverslips with an 18-mm diameter were cleaned by sonication for 30 min in 1 M
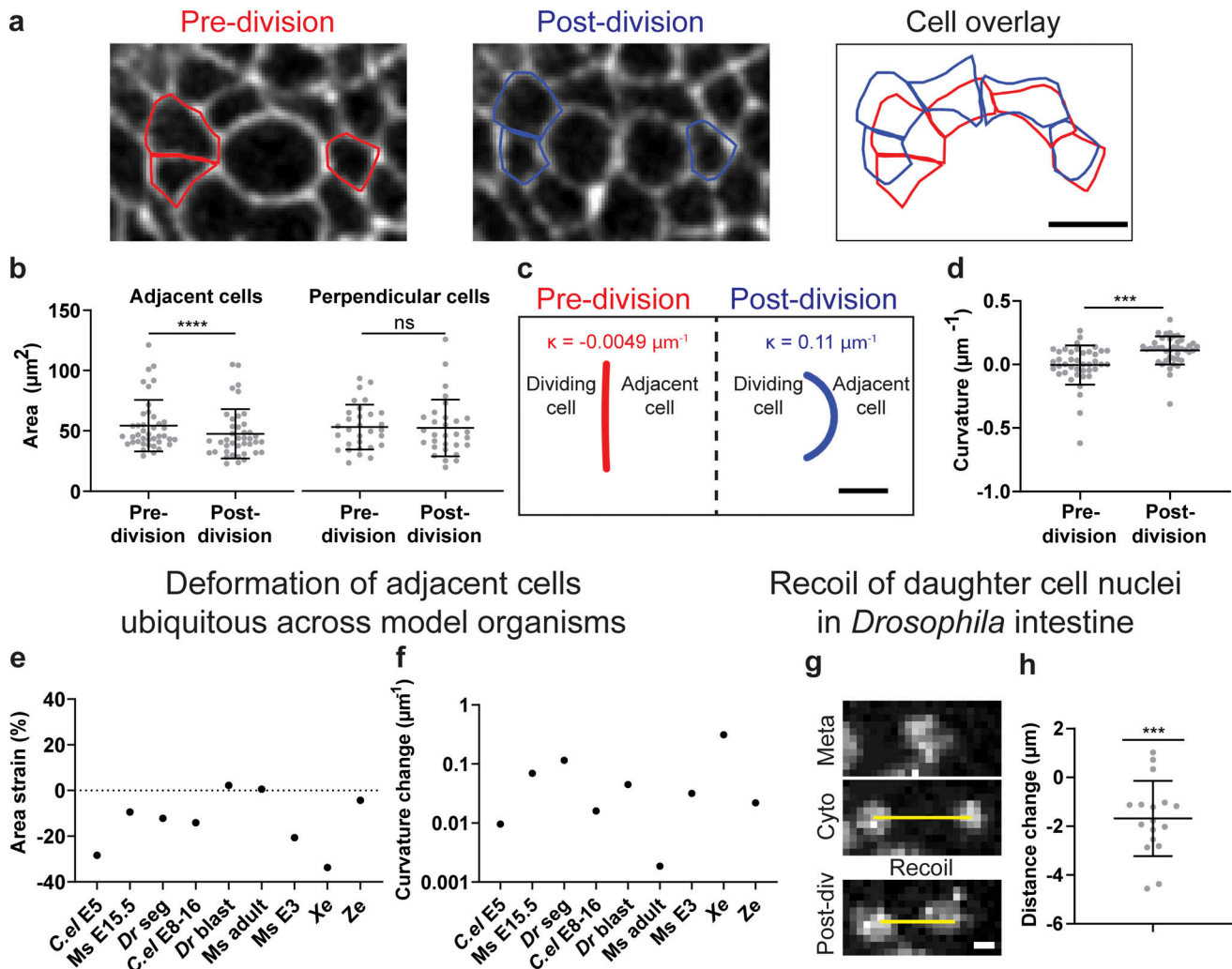
Figure 8. **The forces of division elongation are universal across epithelia in vivo. (a and b)** Deformation of adjacent cells in early *Drosophila* embryos during cell division (a), with quantification of adjacent and perpendicular cell area before and after division (b). Mean ± SD; *n* = 41 adjacent cells, *n* = 30 perpendicular cells (from 26 dividing cells); paired two-sample *t* test. Image in a is of utrophin::GFP, which marks the cell cortex. **(c and d)** Schematic displaying average change in curvature of an adjacent cell during division (c) and quantification of curvatures before and after division (d). Mean ± SD; *n* = 41 adjacent cells (from 26 dividing cells); paired two-sample *t* tests. Scale bars, 10 μm. **(e and f)** Deformation of adjacent cells quantified with area strain (e) and curvature change (f) for *C. elegans* embryo E5 (*C. el* E5; *n* = 1), embryonic (E15.5) mouse epidermis (Ms E15.5; *n* = 2), *Drosophila* embryo segmentation (*Dr* seg; *n* = 2), *C. elegans* embryo E8-16 (*C. el* E8-16; *n* = 1), *Drosophila* embryo after the blastoderm stage (*Dr* blast; *n* = 41), adult mouse intestinal organoid (Ms adult; *n* = 2), embryonic (E3) mouse (Ms E3; *n* = 3), *Xenopus* embryo (*Xe*; *n* = 2), and zebrafish larva epidermis (Ze; *n* = 4). **(g and h)** Change in distance of daughter cell nuclei after division completion within the adult *Drosophila* intestine (g) and their quantification (h). Mean ± SD; *n* = 17; one-sample *t* test. Scale bar, 2.5 μm. ***, P < 0.001; ****, P < 0.0001.

NaOH and made hydrophobic with Rain-x (Amazon) treatment. For 1-kPa gels (used for all monolayer experiments), a stock solution of 1 ml was made with 4% acrylamide, 0.06% bisacrlyamide, and 5.5 μl of 0.5 μm carboxylate-modified fluorescent beads (F8888/F8887; Invitrogen). Single cells were unable to divide on 1-kPa gels and thus were plated on gels previously measured to be 7.43 kPa (10% acrylamide, 0.06% bisacrylamide; Tse and Engler, 2010). Prior to the addition of fluorescent beads, the gel solution was vacuumed and the bead solution was sonicated for 20 min. The gel solution was placed on ice for 5 min to slow down polymerization. To activate polymerization, 10 μl of 100 mg/ml ammonium persulfate (7727-

54-0; Arcos Organics) and 1 μl of N,N,N′,N′-tetramethylethylenediamine (T9281; Sigma-Aldrich) was added. A 20-μl drop of gel solution was deposited at the center of the donut-shaped spacer on the glass bottom, followed by placement of the upper coverslip. Dishes were immediately inverted and centrifuged at 150 *g* for 15 min to force fluorescent beads to the surface of the gel. Gels were allowed to polymerize for an additional 25 min. Following polymerization, upper coverslips and donut-shaped spacers were carefully removed. Gels were rinsed 5 × 5 min in MilliQ water to remove unpolymerized acrylamide. Gels were then functionalized with collagen-1 (354236; Corning) by incubating with 1 mg/ml sulfo-SANPAH (22589; Thermo Fisher

Gupta et al.
Cell division forces in epithelial monolayers

Journal of Cell Biology 12 of 20
https://doi.org/10.1083/jcb.202011106

Scientific) under a 15-W UV lamp for 3.5 min. Gels were quickly rinsed with MilliQ water and incubated with ice-cold 0.2 mg/ml collagen-1 in PBS overnight at 4°C. The following day, gels were rinsed with PBS and incubated in cell growth media for 30 min to equilibrate ion concentrations and allow serum proteins to adsorb to the gel surface. For cell plating, cells were resuspended in low volume (~10 µl) of growth media and deposited directly on the gel surface. Cells were allowed to adhere to the gel surface for 15 min and the cell culture dish was then filled with more growth media.

Polyacrylamide gel mechanical characterization
Elastic modulus was measured using an AR-G2 stress-controlled rheometer (TA Instruments) equipped with a 25-mm bottom and upper plate as described previously (Nam et al., 2016). Polyacrylamide gel solution was deposited on the bottom plate immediately after mixing. The upper plate was lowered to 400 µm above the bottom plate and slowly spun to spread the gel solution to the edges of the two plates. Mineral oil was applied to the edges to minimize evaporation. A cyclic strain with amplitude 0.01 at a frequency of 1 rad/s was applied for 1 h at RT to monitor gel polymerization. The temperature was increased to 37°C and measurements were taken for an additional 15 min. The last 10 recorded values for the storage modulus (G') and loss modulus (G'') were used to calculate the shear modulus (G^*) using $G^* = (G'^2 + G''^2)^{1/2}$. This shear modulus value was then converted to an elastic modulus using a Poisson's ratio of 0.457 (Takigawa et al., 1996).

Functionalization of glass substrates with type I collagen
For experiments not requiring flexible hydrogel substrates, cells were plated on glass conjugated with collagen-1, as described previously (Paszek et al., 2012). Glass substrates were cleaned with incubation in 1 M NaOH for 30 min, followed by 0.5% (3-aminopropyl)trimethoxysilane (281778; Sigma-Aldrich) treatment for 30 min, and 0.5% glutaraldehyde (16020; Electron Microscopy Sciences) treatment for 30 min. Substrates were then incubated with 50 µg/ml collagen-1 (354236; Corning) at 4°C overnight.

Live time-lapse microscopy of cultured cells
Unless stated otherwise, cells were imaged every 1–10 min on a Nikon Ti2-E inverted microscope equipped with an ORCA-Flash sCMOS camera, a 10× plan apochromatic NA 0.45 dry objective or 20× plan apochromatic NA 0.75 dry objective, with a pixel size between 0.33 and 0.67 µm, and NIS-Elements Advanced Research software. For measuring traction and monolayer stresses for MCF10A cells, cells were imaged every 2 min on a Leica SP8 confocal microscope equipped with a PMT Trans detector (158004201; Leica) and HyD detector (158001401; Leica) using a 10× HC PL APO CS NA 0.4 dry objective, with a pixel size of 0.57 µm, and LAS X software. Cells were maintained at 37°C and 5% CO_2 for all live-cell experiments. For monolayer height measurements, imaging of cell–matrix adhesions, laser ablation experiments, 3D imaging of adjacent cell deformation during division, cell volume measurements, and *Drosophila* experiments, different imaging equipment was used, as described in the respective sections.

Live time-lapse microscopy of *Drosophila* early embryos
For live imaging of *Drosophila* early embryos, embryos between 3 and 3.5 h old were dechorionated with 50% bleach, rinsed with water, and mounted dorsal side up onto a slide coated with embryo glue (double-sided scotch tape dissolved in heptane). No. 1.5 coverslips were used as spacers to create a channel for the mounted embryo. The channel was filled with Halocarbon 27 oil (Sigma-Aldrich). Images were taken of the dorsal side of the head of the embryos when cells in mitotic domains 1 and 5 were dividing. Images were acquired on a Zeiss LSM 710 confocal microscope, with a 40×/1.2 apochromatic water objective, an argon ion, 561-nm diode, 594-nm HeNe, and 633-nm HeNe lasers. GFP and mCherry markers were simultaneously excited and detected using band-pass filters set at ~490–565 nm for GFP and ~590–690 nm for mCherry. The pinhole was set between 1 and 2 Airy Units for all images. Cell cortices were visualized using a marker for F-actin, the actin binding domain of utrophin fused to GFP (utrophin::GFP; Rauzi et al., 2010), and microtubules were visualized using tubulin::mCherry.

Traction force microscopy
Cells were removed from gel substrates with 0.5% trypsin-EDTA and reference images of fluorescent beads were taken. Substrate displacements between force and reference gel states were aligned to correct for drift using FIJI (Schindelin et al., 2012) and calculated using particle image velocimetry implemented with the MATLAB application PIVLab (Thielicke and Stamhuis, 2014). Two interrogation windows (64 × 64 and 32 × 32 pixels) with 50% overlap were used for most experiments. For MC10A analysis, the pixel size wasgreater and thus interrogation windows with sizes 32 × 32 and 16 × 16 were used. Displacements were filtered through a Gaussian filter with an SD of 6 µm. Substrate displacements were used to calculate cell–matrix stresses using Fourier transform TFM derived previously by Trepat et al. (2009), with our results matching that of pyTFM, an opensource TFM tool (Bauer et al., 2020).

Monolayer stress microscopy
A MATLAB script was used to implement MSM with a monolayer height of 9 µm (Fig. S3, g and h) following a published protocol (Tambe et al., 2011).

Analysis of cell–matrix and cell–cell stress data
Dividing cells were manually identified using brightfield or phase imaging. Cell division phases were assigned based on the following standards: Start of mitosis—edges of parent cell begin to move inward; metaphase end—chromatids were lined along the metaphase plate; anaphase onset—chromosomes begin separating; late anaphase—chromosomes were moving apart with cytokinetic ring contraction initiated; cytokinesis completion—cytokinetic ring contraction had completed; and end of postdivision spreading—edges of the daughter cells were no longer moving outward. A line was drawn along the major axis of cells at late anaphase to measure the division axis orientation. The corresponding cell–matrix and cell–cell stress data were rotated and centered such that the cell was dividing along the horizontal axis at the center of the map. Data were then fit to

a grid with 8.6-μm spacing (11.4 μm for MCF10A analysis). For each dividing cell, cell–matrix and cell–cell stresses were subtracted at two different time points corresponding to two different cell division stages. Peak traction values were defined as the average of the peak differential stress on the left-hand and right-hand side of the dividing cell, within a 60-μm-diameter region of the dividing cell's center. Center monolayer stress values were defined as the differential stress at the center of the dividing cells. Cell–matrix and cell–cell stress heat maps were generated by averaging the change in stress data from >100 cells.

Monolayer height measurements

MDCK cells stably expressing LifeAct::RFP at varying densities were imaged under cell culture conditions (37°C, 5% CO_2) using a laser scanning confocal (SP8; Leica) equipped with a HyD detector (158001401; Leica), 25× Fluotar VISIR NA 0.95 water immersion objective, and LAS X software. Volumetric stacks were binarized using FIJI (Schindelin et al., 2012). The height of the monolayer at every point was calculated by taking the difference between the maximum and minimum binarized values.

Dividing cell edge or vertex categorization

To determine whether cells divide against two adjacent cell edges, two adjacent cell vertices, or an edge and a vertex, phase imaging of MDCK WT or fluorescent imaging of MDCK E-cadherin::DsRed was performed. Each side of the dividing cell was manually categorized as dividing against a cell edge or vertex.

Truncated E-cadherin experiments

Mosaic monolayers with 5% MDCK cells expressing E-cadherin with a truncated extracellular domain (T151–) as well as 95% WT MDCK cells were formed. Division forces were measured for T151– cells surrounded by neighboring WT cells (experimental group), as well as WT cells surrounded by other WT cells (control group). To minimize the number of adjacent T151– cells formed due to division, an instant monolayer was formed as described previously (Nelson and Veshnock, 1987). T151– cells were incubated with 10 μM CellTracker Red CMTPX dye (C34552; Thermo Fisher Scientific) for 20 min at 37°C before trypsinization to differentiate them from MDCK WT cells. After trypsinization, cells were resuspended in low (5 μM) Ca^{2+} growth media to disrupt cell–cell adhesions and plated at a high (300,000 cells/cm²) density in low Ca^{2+} growth media to form an instant monolayer. After 1 h, cell media was replaced with normal growth media (Ca^{2+} 1.8 mM). Imaging began after an additional hour to allow for the formation of cell–cell adhesions.

Truncated E-cadherin immunostaining and imaging

MDCK WT and T151– monolayers were grown on glass substrates conjugated with collagen-1 using similar methods outlined above in Truncated E-cadherin experiments. Samples were fixed, permeabilized, blocked, and stained using previously published protocols (Lee et al., 2019). Samples were fixed with 4% paraformaldehyde for 20 min at RT followed by permeabilization with 0.5% Triton X-100 in PBS for 20 min. Permeabilized samples were then blocked with blocking buffer (1% BSA, 10% goat serum, 0.3 M glycine, and 0.1% Triton X-100 in PBS) for 1 h. Samples were incubated with a monoclonal rat E-cadherin antibody that specifically binds to the extracellular domain of E-cadherin (U3254; Sigma-Aldrich) at 1:1,600 dilution for 1 h followed by incubation with goat anti-rat Alexa 488- or 555-conjugated secondary antibody (A-11006, and A-21434; Thermo Fisher Scientific) at 1:1,000 dilution for 1 h and then DAPI (D9542; Sigma-Aldrich) at 5 μg/ml for 1 min. During imaging, random fields of view were focused using the nuclear DAPI channel and then imaged on the extracellular E-cadherin channel. For quantification, only fields of view with similar densities between WT and T151– samples were used. The total fluorescence intensity within each image was noted. Total fluorescence intensity for each image was then normalized by the maximum fluorescence intensity within a given replicate (either WT or T151–) to account for differences in output between different imaging sessions.

Neighboring nuclei arrangement, movement, and cross-sectional area change during division

Nuclei were imaged using MDCK cells stably expressing the FUCCI cell cycle reporter. Nuclei images were binarized and segmented using FIJI (Schindelin et al., 2012). Segmented nuclei were then fit to a grid with 20-μm spacing. Cells within one grid spacing and along the division axis were categorized as adjacent cells. Cells within one grid spacing and along the axis perpendicular to the dividing cell were categorized as perpendicular cells. The arrangement of neighboring cells—one grid spacing away—with respect to the dividing cell's orientation was quantified by measuring the angles between the dividing cell at metaphase and neighboring nuclei centroids. Nuclear deformation of cells was quantified by measuring the change in area imaged near the center cross-sectional plane of the cell imaged using wide-field microscopy. Heat maps display the average of neighboring cells' nucleus strain across all observed division events.

Neighboring cell area measurements during division

For in vitro experiments (Fig. 4, a, b, and e), MDCK cells stably expressing Ecad::DsRed or LifeAct::RFP were imaged. Fluorescent images were binarized and segmented using FIJI (Schindelin et al., 2012). Segmented cells were then fit to a grid with 20-μm spacing. Cells within one grid spacing away from the dividing cell and along the division axis were categorized as adjacent cells. Cells within one grid spacing away from the dividing cell and along the perpendicular axis were categorized as perpendicular cells. Cells within 100 μm of the dividing cell were categorized as far cells. Deformation of cells was quantified by measuring the change in cross-sectional area imaged near the center plane of the dividing cell using wide-field microscopy. Heat maps display neighboring cells' area strains averaged across all observed division events. For analysis of cell division within early *Drosophila* embryos after the blastoderm stage (mitotic domains 1 and 5; Fig. 8, a and b), due to the large number of dividing cells within the same region, adjacent or perpendicular cells that had recently divided or were undergoing division soon after were excluded. Analysis was conducted based on images taken at the center of the dividing cell imaged using laser scanning confocal microscopy. For images displayed from in vivo model systems (Fig. 8 e), fluorescent images of a

single dividing cell with a cell membrane marker from various model systems were taken from previously published papers (Niwayama et al., 2019; Foe, 1989; Gudipaty et al., 2017; Miroshnikova et al., 2018; McKinley et al., 2018; Scarpa et al., 2018; Kieserman and Wallingford, 2009; Bai et al., 2020). The model systems used consisted of embryonic (E15.5) mouse epidermis, *Drosophila* embryo during segmentation, *Drosophila* embryo after the blastoderm stage, adult mouse intestinal organoid, embryonic (E3) mouse, *Xenopus* embryo during neural tube closure, *C. elegans* embryo (E5), *C. elegans* embryo intestine (E8–E16), and zebrafish larva epidermis. Images were analyzed similarly but with manual outlining. Area strains displayed are from a single division event and average measurements from 1 to 4 adjacent cells. For the analysis of zebrafish larvae epidermis, image scale was estimated based on another image of zebrafish (Gudipaty et al., 2017).

Curvature (κ) measurements of cell–cell boundaries during division

Common boundary points between the dividing cell and neighboring cells were noted. If the angle between the division axis and the axis defined by a daughter cell's centroid and the centroid of the common boundary points was less than 100°, the neighboring cell was considered to be an adjacent cell. Common points between the dividing cell and an adjacent cell were fit to a circle using code from the MATLAB central file exchange using least-squares fitting (Pratt, 1987; Chernov, 2020). The inverse of the radius of the fitted circle was taken to be the curvature value. If the center of the fitted circle was not in the direction of the dividing cell, the curvature was taken to be negative. Representative arcs were drawn at arbitrary spacing, with arbitrary but equal lengths between the two time points compared, and with average curvature values of measured data.

Adhesion imaging and tracking

To image and track adhesions, total internal reflection microscopy was performed under cell culture conditions (37°C, 5% CO_2) using a Nikon Eclipse-TI inverted microscope equipped with a Plan Apo-total internal reflection microscopy 100× 1.49-NA oil immersion objective, Andor Neo sCMOS camera, and NIS-Elements Advanced Research. Adhesions of dividing and neighboring cells were imaged using MDCK cells stably expressing vinculin::GFP. For each dividing cell, adhesions within a 50 × 30-µm (longer dimension oriented along division axis) area were tracked as the dividing cell transitions from metaphase to cytokinesis completion. The open-source Focal Adhesion Analysis Server was used to identify adhesions (Berginski and Gomez, 2013). We measured the number of adhesions identified when the dividing cell reaches metaphase and cytokinesis completion.

3D live-cell division imaging and measuring distance to dividing cell edge at the basal plane

Mosaic monolayers were formed using 50% MDCK cells stably expressing LifeAct::RFP and 50% MDCK cells stably expressing LifeAct::GFP. Time-lapse images of dividing cells were taken using either a Nikon Ti2-E inverted microscope equipped with a X-Light V2 spinning disk (40× Apochromatic NA 1.15 water immersion objective, ORCA-Flash sCMOS camera, NIS-Elements Advanced Research software) or a Leica SP8 confocal microscope (25× Fluotar VISIR NA 0.95 water immersion objective, Leica HyD detector; part #158001401; LAS X software) under cell culture conditions (37°C, 5% CO_2). Cells at cytokinesis completion were identified, and the distance along the division axis between the center of the daughter cell pair to the adjacent cell edge was manually measured at the basal plane.

Estimating division elongation forces using adjacent cell deformation

From 3D time-course imaging of mosaic monolayers expressing LifeAct, cells adjacent to dividing cells were manually outlined at metaphase and cytokinesis completion. Distribution of coordinates was sorted clockwise along with the curvature, after which slices were smoothed to eliminate sharp edges and corners using Savitzky-Golay filtering (MATLAB and Signal Processing Toolbox). A 3D loft feature was constructed by stacking all slices, the coordinates of which were extracted in Abaqus (Abaqus, 2020; Dassault Systèmes). Coordinates were upscaled by three orders of magnitude or features were magnified by nine orders of magnitude in volume to facilitate 3D file transfer across various simulation tools. Cells were assumed to be isotropic, with a 1-kPa Young's modulus, 1,000 kg/m³ density, and 0.38 Poisson's ratio (Brückner et al., 2017; Trickey et al., 2006). The geometry was imported to Ansys and undeformed faces were assumed to be fixed, with frictionless movement at the top and bottom faces permitted. Five different force magnitudes (10 nN, 50 nN, 100 nN, 300 nN, and 500 nN) were loaded and oriented in the direction of the most pronounced cell deformation, while maintaining equivalent boundary conditions across simulations with varying forces. Forces implemented in the simulation were upscaled by six orders of magnitude to accommodate the length upscale. Due to the relatively high resolution of coordinate sets extracted from the 3D model compared with imaging resolution, coordinates with the least distance from experimental data were extracted, from which the structural similarity (structural similarity index measure [SSIM]) across all z slices was computed in MATLAB. SSIM values were then normalized by SSIM values calculated for the undeformed (0 nN) case by taking the difference between the SSIM value at a particular force value and SSIM at 0 nN and dividing by the difference between 1 and the SSIM value at 0 nN. Normalized SSIM values were compared between different force values for all z slices.

Pharmacological inhibition experiments to assess the role of interpolar spindle elongation and cytokinetic ring contraction

Cell elongation and interpolar spindle elongation during division was measured by imaging MDCK cells stably expressing either E-cadherin::DsRed or LifeAct::RFP, and α-tubulin::GFP, respectively. Chromosome segregation was visualized using brightfield imaging. Blebbistatin (100 µM; 203389; Sigma-Aldrich), BRD9876 (40 µM; 9876; Tocris) and S-trityl-L-cysteine (25 µM; 164739; Sigma-Aldrich), and BTO-1 (50 µM; B6311; Sigma-Aldrich) were used to inhibit myosin II, kinesin-5, and polo-like kinase 1, respectively (Chattopadhyay et al., 2015; Straight et al.,

2003; Brennan et al., 2007; DeBonis et al., 2004; Skoufias et al., 2006). To specifically evaluate the contribution of interpolar spindle elongation and cytokinetic ring contraction during division elongation, only cells that had progressed to metaphase after the drug was added were analyzed. Only fields of view with similar monolayer densities were compared between control and experimental conditions. To assess the role of interpolar spindle elongation, cell elongation was measured 6 min after anaphase onset, and to assess the role of cytokinesis, cell elongation was measured 8–10 min after anaphase onset. For those cells treated with blebbistatin or BTO-1, only cells that failed to complete cytokinesis and had become binucleate were considered. Reduction in cell elongation was defined as the percent difference in mean cell elongation from experimental and control conditions normalized to the control condition.

Anillin knockdown

Knockdown of anillin within MCF10A cells stably expressing LifeAct::RFP was accomplished using Dharmacon ON-TARGETplus human anillin siRNA set of 4 (LQ-006838-00-0002). Target sequences were as follows: (1) 5′-GCAAACAACUAGAAACCAA-3′, (2) 5′-GGCGAUGCCUCUUUGAAUA-3′, (3) 5′-GAUCAAGCA UUAGCAGAAA-3′, and (4) 5′-ACGCAACACUUUUGAAUUA-3′. A nontargeting siRNA was used as a control (CTRL). Cells were transfected with a final siRNA concentration of 20 nM using Dharmacon 1 reagent. Cells were imaged and assayed for Western blot 24–48 h after transfection. Cell division within both control and experimental groups was slightly delayed, and thus cell elongation was measured 12 min after anaphase onset. Within the siANLN experimental group, only dividing cells that resulted in cytokinesis failure were considered. For correlation between cytokinetic ring contraction and cell elongation within siANLN dividing cells, minimum cell width was measured along the cytokinetic ring, and cell elongation was measured at the time cytokinetic ring contraction reached a minimum.

Western blot of anillin knockdown

Cells transfected were lysed and denatured, followed by gel electrophoresis, transfer to nitrocellulose, blocking, primary antibody incubation, and secondary antibody incubation following previously published protocols (Lee et al., 2019). Cells transfected with siCTRL or siANLN were lysed with radioimmunoprecipitation assay buffer (89901; Thermo Fisher Scientific) supplemented with phosphatase (04906845001; Roche) and protease (05892791001; Roche) inhibitors. A bicinchoninic acid assay (23227; Thermo Fisher Scientific) was performed to determine protein concentration, and lysates were diluted to 5 µg/ml protein concentration using Laemmli sample buffer (1610747; Bio-Rad). Samples were boiled for 10 min to denature proteins. A 4% to 15% SDS-PAGE gel (4561086; Bio-Rad) and transfer to nitrocellulose membrane was run with 50 µg of total protein per lane and a prestained protein ladder (928–60000; Li-Cor Biosciences). Membranes were blocked with 5% nonfat milk in TBS-Tween 20 for 30 min and incubated with primary rabbit anillin antibody at 200 ng/ml in TBS-Tween 20 overnight (A301-405A; Bethyl Laboratories) and IRDye 800-conjugated donkey secondary antibody (926–32213; Li-Cor Biosciences) at

1:10,000 dilution in blocking buffer for 1 h. Membranes were imaged using a Li-COR Odyssey imaging system. Protein concentration was compared by normalizing experimental band intensity to control intensity (relative density), and then normalizing the anillin relative density to that of a loading control (GAPDH; 181602; Abcam), which was imaged at a lower intensity to avoid saturation.

Laser ablation

Laser ablation was performed on a laser scanning confocal microscope (Zeiss LSM 780) at the Stanford Cell Sciences Imaging Facility using a Mai Tai DeepSee (Spectra Physics) multiphoton laser (800-nm wavelength), 40× C-APO NA 1.2 water immersion objective, 32 anode Hybrid-GaAsP detector, standard fluorescent photomultiplier tube, and Zen Black software. MDCK cells stably expressing α-tubulin::GFP were maintained in cell culture conditions at 37°C with 5% CO_2. After identifying dividing cells in late anaphase, a region of interest at the center of the dividing cell was drawn. Ablation was performed by scanning the multiphoton laser within the region of interest at five to seven z-planes (1–2 µm apart) spanning the thickness of the dividing cell. Before and after ablation images were taken at the center plane. Change in distance between the dividing cell's chromosomes and length were measured, with negative values indicating inward movement of the chromosome pair, or cell shortening, and positive values indicating outward movement of the chromosome pair, or cell elongation. For 3D membrane imaging, cells were stained with CellMask orange plasma membrane stain (C10045; Thermo Fisher Scientific) at 5 µg/ml for 10 min before imaging. Before and after ablation, z-stacks were taken with 0.75–1-µm spacing between z-slices. Images displayed are side-view images of the dividing cell's center (Fig. S4 a). The boundary of the dividing cell at pre- and postablation time points was outlined for comparison.

Cell volume measurements

MDCK cells stably expressing LifeAct::GFP or LifeAct::RFP were imaged under cell culture conditions (37°C, 5% CO_2) on a laser scanning confocal (SP8; Leica) using a 25× Fluotar VISIR NA 0.95 water immersion objective, HyD detector (part #158001401; Leica), and LAS X software. Cells at metaphase were identified using a nuclear stain (R37106; Thermo Fisher Scientific). Volumetric stacks were taken immediately after anaphase onset, at the start of cytokinesis, and upon cytokinesis completion. Cell volume was measured by calculating the number of voxels within the cell region by manually outlining the dividing cell at each imaging plane.

Computational modeling of cell elongation during cytokinesis
Summary

Using a computational model, we evaluated how much a cell can be elongated in the axial direction due to a contractile force exerted on the equator of the cell. The cell is simplified into a 3D structure comprised of a membrane with conservation of volume and area. The membrane is coarse grained using a triangulated mesh, as in previous works (Fedosov, 2010). The number of nodes comprising the membrane mesh is 10,242, and the initial length of chains between adjacent nodes is ~0.5 µm.

Extensional stiffness prevents chains between nodes on the mesh from elongating or shortening to a large extent. Bending stiffness maintains a dihedral angle formed by adjacent triangles on the mesh near equilibrium level. Volume encapsulated by the membrane and the total surface area of the membrane are maintained near their initial values to various extents. The membrane initially has a spherical shape the radius of which is 10 µm. To mimic the constriction of a cytokinetic ring, membrane nodes located near the equator are displaced at constant speed (Fig. 7 c). Consequently, the narrow region contracts toward the cytokinetic axis as the constricting ring observed during cytokinesis. We ran simulations with different strengths of volume and area conservation and measured how much the cell-like structure is elongated in the axial direction.

Brownian dynamics with the Langevin equation

Displacements of membrane nodes are determined by the Langevin equation with inertia neglected:

$$\mathbf{F}_i - \zeta_i \frac{d\mathbf{r}_i}{dt} + \mathbf{F}_i^T = 0, \tag{1}$$

where $\mathbf{r}_i$ is a position vector of the ith node, ζ_i is a drag coefficient, t is time, $\mathbf{F}_i$ is a deterministic force, and $\mathbf{F}_i^T$ is a stochastic force satisfying the fluctuation-dissipation theorem (Underhill and Doyle, 2004):

$$\left\langle \mathbf{F}_i^T(t)\mathbf{F}_j^T(t) \right\rangle = \frac{2k_B T \zeta_i \delta_{ij}}{\Delta t} \boldsymbol{\delta}, \tag{2}$$

where δ_{ij} is the Kronecker delta, $\boldsymbol{\delta}$ is a second-order tensor, and Δt is a time step.

The drag coefficients of membrane nodes are calculated as follows:

$$\zeta_i = \lambda A_i, \tag{3}$$

where λ is a constant and A_i is the instantaneous area of a pentagon or a hexagon whose center corresponds to a node i (Fig. S4 b).

Positions of all nodes are updated via Euler integration scheme:

$$\mathbf{r}_i(t + \Delta t) = \mathbf{r}_i(t) + \frac{d\mathbf{r}_i}{dt}\Delta t = \mathbf{r}_i(t) + \frac{1}{\zeta_i}\left(\mathbf{F}_i + \mathbf{F}_i^T\right)\Delta t. \tag{4}$$

Extensional and bending forces

Extensional stiffness (κ_s) keeps the chain length between nodes within a given range. It is allowed to vary between 0.05 µm and 1.25 µm without resistance, but if the chain length increases or decreases beyond the range, a linear spring force is applied to bring it back within the range. Thus, the potential function (U_s) for the chain extension is:

$$U_s = \begin{cases} \frac{1}{2}\kappa_s(r - r_{0,L})^2 & \text{if } r < r_{0,L} \\ 0 & \text{if } r_{0,L} \leq r \leq r_{0,H} \\ \frac{1}{2}\kappa_s(r - r_{0,H})^2 & \text{if } r > r_{0,H} \end{cases}, \tag{5}$$

where r is instantaneous chain length and $r_{0,L}$ and $r_{0,H}$ are the lower and upper limits of the range, respectively.

Bending stiffness (κ_b) maintains a dihedral angle (θ) formed by two adjacent triangles located on the mesh near equilibrium level ($\theta_0 = 0$ rad):

$$U_b = \kappa_b[1 - \cos(\theta - \theta_0)]. \tag{6}$$

Forces calculated from U_b are applied to four nodes that constitute the two adjacent triangles.

Conservation of volume and surface area

Volume encapsulated by the membrane is conserved by the following potential (U_v):

$$U_v = \frac{\kappa_v(V - V_0)^2}{2V_0}, \tag{7}$$

where κ_v is the strength of volume conservation and V and V_0 are instantaneous and equilibrium volume within the membrane, respectively. The global volume is calculated by summing the volume of tetrahedra, each of which is defined by three nodes of a triangle on the mesh and the center point of the membrane. To maintain V near V_0, forces calculated from U_v move triangles on the mesh outward or inward in directions normal to the triangles. For example, if V is smaller than V_0, forces are applied to membrane nodes to push triangles on the mesh outward so that V can increase.

The global surface area of the membrane is conserved by another potential (U_a):

$$U_a = \frac{\kappa_a(A - A_0)^2}{2A_0}, \tag{8}$$

where κ_a is the strength of area conservation and A and A_0 are instantaneous and equilibrium surface area, respectively. Forces calculated from U_a make individual triangles larger or smaller to maintain A near A_0. For example, if A is smaller than A_0, forces are applied to membrane nodes to make triangles larger so that A can increase. It has been shown that the surface area of cells can be increased due to membrane reservoirs (Gauthier et al., 2011; Raucher and Sheetz, 1999), whereas lipid vesicles commonly used for in vitro experiments cannot accommodate a large change in the surface area due to the absence of membrane reservoirs.

Simulation setup

In each simulation, a spherical membrane the radius of which is 10 µm is located at the center of a large 3D domain (100 × 100 × 100 µm). To mimic the constriction of a cytokinetic ring, 522 membrane nodes within a region the width of which is 1 µm near the equator of the membrane are displaced inward toward the cytokinetic axis at a constant speed, v_c (Fig. 7 c). Those membrane nodes stop being displaced after a distance to the cytokinetic axis becomes less than 0.5 µm. Consequently, the narrow region contracts toward the cytokinetic axis as the constricting ring observed during cytokinesis.

We ran simulations with different strengths of volume and area conservation and evaluated how much the cell-like structure is elongated in the axial direction. The extent of cell elongation is defined by dividing the distance between the leftmost and rightmost points of the membrane by the initial diameter of the membrane.

Calculation of nuclei recoil distance in adult *Drosophila* intestine

Images of nuclei within the intestine of adult *Drosophila* were taken from previously published data (Martin et al., 2018). The nuclei of dividing mother stem cell and resulting daughter stem cells were segmented using Imaris. The difference in distances of daughter cell's nuclei centroids between division completion and 7.5 min later was calculated.

Statistics

All statistical analysis and graphical figures were done using GraphPad Prism or MATLAB. All statistical tests used and information on replicates is summarized in Table S1. For graphs with error bars, the center bar indicates mean and upper and lower bars indicate SD. All data points within different replicates were combined before statistical tests were performed. Data distributions were assumed to be normal, but this was not statistically tested.

Online supplemental material

Fig. S1 displays MDCK epithelial cell division accompanied by distinct stages of cell–cell stress. Fig. S2 displays MCF10A epithelial cell division accompanied by distinct stages of cell–matrix and cell–cell stress. Fig. S3 shows the effect of epithelial monolayer density on measured cell division stresses and that observed stresses are specific for only dividing cells in the monolayer. Fig. S4 shows that the interpolar spindle does not bear compressive forces during division elongation, while varying levels of volume conservation during cytokinesis leads to cell elongation. Fig. S5 shows cells being deformed during division elongation within various epithelia in vivo, suggesting that forces of division elongation are universal across epithelia. Table S1 lists information on replicates, number of data points, and statistical testing. Table S2 lists parameters employed in the computational model of cell elongation during cytokinesis (Fig. 7, b–e; and Fig. S4, b–f). Supplemental references cite works referred to within the Supplemental Materials.

Data availability

The main data supporting the results presented are available within the paper and all other data and code are available from the corresponding author upon request.

References

Aratyn-Schaus, Y., P.W. Oakes, J. Stricker, S.P. Winter, and M.L. Gardel. 2010. Preparation of complaint matrices for quantifying cellular contraction. *J. Vis. Exp.* 46:e2173. https://doi.org/10.3791/2173

Bai, X., M. Melesse, C.G. Sorensen Turpin, D.E. Sloan, C.Y. Chen, W.C. Wang, P.Y. Lee, J.R. Simmons, B. Nebenfuehr, D. Mitchell, et al. 2020. Aurora B functions at the apical surface after specialized cytokinesis during morphogenesis in *C. elegans*. *Development*. 147:dev181099. https://doi.org/10.1242/dev.181099

Bauer, A., M. Prechová, M. Gregor, and B. Fabry. 2020. pyTFM: A tool for Traction Force and Monolayer Stress Microscopy. *bioRxiv*. 2020.09.28.316430.

Berginski, M.E., and S.M. Gomez. 2013. The focal adhesion analysis server : a web tool for analyzing focal adhesion dynamics. *F1000Research*. 2. doi:. https://doi.org/10.12688/f1000research.2-68.v1

Borghi, N., M. Sorokina, O.G. Shcherbakova, W.I. Weis, B.L. Pruitt, W.J. Nelson, and A.R. Dunn. 2012. E-cadherin is under constitutive actomyosin-generated tension that is increased at cell-cell contacts upon externally applied stretch. *Proc. Natl. Acad. Sci. USA*. 109:12568–12573. https://doi.org/10.1073/pnas.1204390109

Brennan, I.M., U. Peters, T.M. Kapoor, and A.F. Straight. 2007. Polo-like kinase controls vertebrate spindle elongation and cytokinesis. *PLoS One*. 2:e409. https://doi.org/10.1371/journal.pone.0000409

Brückner, B.R., H. Nöding, and A. Janshoff. 2017. Viscoelastic Properties of Confluent MDCK II Cells Obtained from Force Cycle Experiments. *Biophys. J.* 112:724–735. https://doi.org/10.1016/j.bpj.2016.12.032

Cattin, C.J., M. Düggelin, D. Martinez-Martin, C. Gerber, D.J. Müller, and M.P. Stewart. 2015. Mechanical control of mitotic progression in single animal cells. *Proc. Natl. Acad. Sci. USA*. 112:11258–11263. https://doi.org/10.1073/pnas.1502029112

Chattopadhyay, S., A.L. Stewart, S. Mukherjee, C. Huang, K.A. Hartwell, P.G. Miller, R. Subramanian, L.C. Carmody, R.Z. Yusuf, D.B. Sykes, et al.

2015. Niche-based screening in multiple myeloma identifies a kinesin-5 inhibitor with improved selectivity over hematopoietic progenitors. *Cell Rep.* 10:755–770. https://doi.org/10.1016/j.celrep.2015.01.017

Chernov, N. 2020. Circle fit (Pratt method). MATLAB Central File Exchange. https://www.mathworks.com/matlabcentral/fileexchange/22643-circle-fit-pratt-method (accessed May 13, 2020).

Cramer, L.P., and T.J. Mitchison. 1995. Myosin is involved in postmitotic cell spreading. *J. Cell Biol.* 131:179–189. https://doi.org/10.1083/jcb.131.1.179

da Silva, S.M., and J.P. Vincent. 2007. Oriented cell divisions in the extending germband of Drosophila. *Development.* 134:3049–3054. https://doi.org/10.1242/dev.004911

Debnath, J., S.K. Muthuswamy, and J.S. Brugge. 2003. Morphogenesis and oncogenesis of MCF-10A mammary epithelial acini grown in three-dimensional basement membrane cultures. *Methods.* 30:256–268. https://doi.org/10.1016/S1046-2023(03)00032-X

DeBonis, S., D.A. Skoufias, L. Lebeau, R. Lopez, G. Robin, R.L. Margolis, R.H. Wade, and F. Kozielski. 2004. In vitro screening for inhibitors of the human mitotic kinesin Eg5 with antimitotic and antitumor activities. *Mol. Cancer Ther.* 3:1079–1090.

Dix, C.L., H.K. Matthews, M. Uroz, S. McLaren, L. Wolf, N. Heatley, Z. Win, P. Almada, R. Henriques, M. Boutros, et al. 2018. The role of mitotic cell-substrate adhesion re-modeling in animal cell division. *Dev. Cell.* 45:132–145.e3. https://doi.org/10.1016/j.devcel.2018.03.009

Doostmohammadi, A., S.P. Thampi, T.B. Saw, C.T. Lim, B. Ladoux, and J.M. Yeomans. 2015. Celebrating Soft Matter's 10th Anniversary: Cell division: a source of active stress in cellular monolayers. *Soft Matter.* 11:7328–7336. https://doi.org/10.1039/C5SM01382H

Fedosov, D.A. 2010. Multiscale modeling of blood flow and soft matter. PhD thesis. Brown University, Providence, RI. 291 pp.

Fink, J., N. Carpi, T. Betz, A. Bétard, M. Chebah, A. Azioune, M. Bornens, C. Sykes, L. Fetler, D. Cuvelier, and M. Piel. 2011. External forces control mitotic spindle positioning. *Nat. Cell Biol.* 13:771–778. https://doi.org/10.1038/ncb2269

Firmino, J., D. Rocancourt, M. Saadaoui, C. Moreau, and J. Gros. 2016. Cell division drives epithelial cell rearrangements during gastrulation in chick. *Dev. Cell.* 36:249–261. https://doi.org/10.1016/j.devcel.2016.01.007

Foe, V.E. 1989. Mitotic domains reveal early commitment of cells in Drosophila embryos. *Development.* 107:1–22. https://doi.org/10.1242/dev.107.1.1

Freddo, A.M., S.K. Shoffner, Y. Shao, K. Taniguchi, A.S. Grosse, M.N. Guysinger, S. Wang, S. Rudraraju, B. Margolis, K. Garikipati, et al. 2016. Coordination of signaling and tissue mechanics during morphogenesis of murine intestinal villi: a role for mitotic cell rounding. *Integr. Biol.* 8:918–928. https://doi.org/10.1039/C6IB00046K

Gauthier, N.C., M.A. Fardin, P. Roca-Cusachs, and M.P. Sheetz. 2011. Temporary increase in plasma membrane tension coordinates the activation of exocytosis and contraction during cell spreading. *Proc. Natl. Acad. Sci. USA.* 108:14467–14472. https://doi.org/10.1073/pnas.1105845108

Gudipaty, S.A., J. Lindblom, P.D. Loftus, M.J. Redd, K. Edes, C.F. Davey, V. Krishnegowda, and J. Rosenblatt. 2017. Mechanical stretch triggers rapid epithelial cell division through Piezo1. *Nature.* 543:118–121. https://doi.org/10.1038/nature21407

Guillot, C., and T. Lecuit. 2013. Mechanics of epithelial tissue homeostasis and morphogenesis. *Science.* 340:1185–1189. https://doi.org/10.1126/science.1235249

Guo, W.H., and Y.L. Wang. 2011. Micropatterning cell-substrate adhesions using linear polyacrylamide as the blocking agent. *Cold Spring Harb. Protoc.* 2011:prot5582. https://doi.org/10.1101/pdb.prot5582

Hart, K.C., J. Tan, K.A. Siemers, J.Y. Sim, B.L. Pruitt, W.J. Nelson, and M. Gloerich. 2017. E-cadherin and LGN align epithelial cell divisions with tissue tension independently of cell shape. *Proc. Natl. Acad. Sci. USA.* 114:E5845–E5853. https://doi.org/10.1073/pnas.1701703114

Hoijman, E., D. Rubbini, J. Colombelli, and B. Alsina. 2015. Mitotic cell rounding and epithelial thinning regulate lumen growth and shape. *Nat. Commun.* 6:7355. https://doi.org/10.1038/ncomms8355

Kieserman, E.K., and J.B. Wallingford. 2009. In vivo imaging reveals a role for Cdc42 in spindle positioning and planar orientation of cell divisions during vertebrate neural tube closure. *J. Cell Sci.* 122:2481–2490. https://doi.org/10.1242/jcs.042135

Ko, C.S., P. Kalakuntla, and A.C. Martin. 2020. Apical constriction reversal upon mitotic entry underlies different morphogenetic outcomes of cell division. *Mol. Biol. Cell.* 31:1663–1674. https://doi.org/10.1091/mbc.E19-12-0673

Kondo, T., and S. Hayashi. 2013. Mitotic cell rounding accelerates epithelial invagination. *Nature.* 494:125–129. https://doi.org/10.1038/nature11792

Krndija, D., F. El Marjou, B. Guirao, S. Richon, O. Leroy, Y. Bellaiche, E. Hannezo, and D.M. Vignjevic. 2019. Active cell migration is critical for steady state epithelial turnover in the gut. *Science.* 365:705–710.

Lancaster, O.M., M. Le Berre, A. Dimitracopoulos, D. Bonazzi, E. Zlotek-Zlotkiewicz, R. Picone, T. Duke, M. Piel, and B. Baum. 2013. Mitotic rounding alters cell geometry to ensure efficient bipolar spindle formation. *Dev. Cell.* 25:270–283. https://doi.org/10.1016/j.devcel.2013.03.014

Lee, J.Y., J.K. Chang, A.A. Dominguez, H.P. Lee, S. Nam, J. Chang, S. Varma, L.S. Qi, R.B. West, and O. Chaudhuri. 2019. YAP-independent mechanotransduction drives breast cancer progression. *Nat. Commun.* 10:1848. https://doi.org/10.1038/s41467-019-09755-0

Maddox, A.S., and K. Burridge. 2003. RhoA is required for cortical retraction and rigidity during mitotic cell rounding. *J. Cell Biol.* 160:255–265. https://doi.org/10.1083/jcb.200207130

Mammoto, A., T. Mammoto, and D.E. Ingber. 2012. Mechanosensitive mechanisms in transcriptional regulation. *J. Cell Sci.* 125:3061–3073. https://doi.org/10.1242/jcs.093005

Martin, J.L., E.N. Sanders, P. Moreno-Roman, L.A. Jaramillo Koyama, S. Balachandra, X. Du, and L.E. O'Brien. 2018. Long-term live imaging of the *Drosophila* adult midgut reveals real-time dynamics of division, differentiation and loss. *eLife.* 7:e36248. https://doi.org/10.7554/eLife.36248

McKinley, K.L., N. Stuurman, L.A. Royer, C. Schartner, D. Castillo-Azofeifa, M. Delling, O.D. Klein, and R.D. Vale. 2018. Cellular aspect ratio and cell division mechanics underlie the patterning of cell progeny in diverse mammalian epithelia. *eLife.* 7:e36739. https://doi.org/10.7554/eLife.36739

Miroshnikova, Y.A., H.Q. Le, D. Schneider, T. Thalheim, M. Rübsam, N. Bremicker, J. Polleux, N. Kamprad, M. Tarantola, I. Wang, et al. 2018. Adhesion forces and cortical tension couple cell proliferation and differentiation to drive epidermal stratification. *Nat. Cell Biol.* 20:69–80. https://doi.org/10.1038/s41556-017-0005-z

Nam, S., and O. Chaudhuri. 2018. Mitotic cells generate protrusive extracellular forces to divide in three-dimensional microenvironments. *Nat. Phys.* 14:621–628. https://doi.org/10.1038/s41567-018-0092-1

Nam, S., K.H. Hu, M.J. Butte, and O. Chaudhuri. 2016. Strain-enhanced stress relaxation impacts nonlinear elasticity in collagen gels. *Proc. Natl. Acad. Sci. USA.* 113:5492–5497. https://doi.org/10.1073/pnas.1523906113

Nelson, W.J., and P.J. Veshnock. 1987. Modulation of fodrin (membrane skeleton) stability by cell-cell contact in Madin-Darby canine kidney epithelial cells. *J. Cell Biol.* 104:1527–1537. https://doi.org/10.1083/jcb.104.6.1527

Niwayama, R., P. Moghe, Y.-J. Liu, D. Fabrèges, F. Buchholz, M. Piel, and T. Hiiragi. 2019. A tug-of-war between cell shape and polarity controls division orientation to ensure robust patterning in the mouse blastocyst. *Dev. Cell.* 51:564–574.e6. https://doi.org/10.1016/j.devcel.2019.10.012

Parker, A., O.J. Maclaren, A.G. Fletcher, D. Muraro, P.A. Kreuzaler, H.M. Byrne, P.K. Maini, A.J.M. Watson, and C. Pin. 2017. Cell proliferation within small intestinal crypts is the principal driving force for cell migration on villi. *FASEB J.* 31:636–649. https://doi.org/10.1096/fj.201601002

Paszek, M.J., C.C. DuFort, M.G. Rubashkin, M.W. Davidson, K.S. Thorn, J.T. Liphardt, and V.M. Weaver. 2012. Scanning angle interference microscopy reveals cell dynamics at the nanoscale. *Nat. Methods.* 9:825–827. https://doi.org/10.1038/nmeth.2077

Plotnikov, S.V., B. Sabass, U.S. Schwarz, and C.M. Waterman. 2014. High-resolution traction force microscopy. *Methods Cell Biol.* 123:367–394. https://doi.org/10.1016/B978-0-12-420138-5.00020-3

Pratt, V. 1987. Direct least-squares fitting of algebraic surfaces. *SIGGRAPH '87: Proceedings of the 14th annual conference on Computer graphics and interactive techniques.* 145–152. https://doi.org/10.1145/37402.37420

Przybyla, L., J.N. Lakins, R. Sunyer, X. Trepat, and V.M. Weaver. 2016. Monitoring developmental force distributions in reconstituted embryonic epithelia. *Methods.* 94:101–113. https://doi.org/10.1016/j.ymeth.2015.09.003

Raucher, D., and M.P. Sheetz. 1999. Characteristics of a membrane reservoir buffering membrane tension. *Biophys. J.* 77:1992–2002. https://doi.org/10.1016/S0006-3495(99)77040-2

Rauzi, M., P.F. Lenne, and T. Lecuit. 2010. Planar polarized actomyosin contractile flows control epithelial junction remodelling. *Nature.* 468:1110–1114. https://doi.org/10.1038/nature09566

Rosa, A., E. Vlassaks, F. Pichaud, and B. Baum. 2015. Ect2/Pbl acts via Rho and polarity proteins to direct the assembly of an isotropic actomyosin cortex upon mitotic entry. *Dev. Cell.* 32:604–616. https://doi.org/10.1016/j.devcel.2015.01.012

Rossen, N.S., J.M. Tarp, J. Mathiesen, M.H. Jensen, and L.B. Oddershede. 2014. Long-range ordered vorticity patterns in living tissue induced by cell division. *Nat. Commun.* 5:5720. https://doi.org/10.1038/ncomms6720

Scarpa, E., C. Finet, G.B. Blanchard, and B. Sanson. 2018. Actomyosin-driven tension at compartmental boundaries orients cell division independently of cell geometry in vivo. *Dev. Cell.* 47:727–740.e6. https://doi.org/10.1016/j.devcel.2018.10.029

Schindelin, J., I. Arganda-Carreras, E. Frise, V. Kaynig, M. Longair, T. Pietzsch, S. Preibisch, C. Rueden, S. Saalfeld, B. Schmid, et al. 2012. Fiji: an open-source platform for biological-image analysis. *Nat. Methods.* 9: 676–682. https://doi.org/10.1038/nmeth.2019

Skoufias, D.A., S. DeBonis, Y. Saoudi, L. Lebeau, I. Crevel, R. Cross, R.H. Wade, D. Hackney, and F. Kozielski. 2006. S-trityl-L-cysteine is a reversible, tight binding inhibitor of the human kinesin Eg5 that specifically blocks mitotic progression. *J. Biol. Chem.* 281:17559–17569. https://doi.org/10.1074/jbc.M511735200

Sorce, B., C. Escobedo, Y. Toyoda, M.P. Stewart, C.J. Cattin, R. Newton, I. Banerjee, A. Stettler, B. Roska, S. Eaton, et al. 2015. Mitotic cells contract actomyosin cortex and generate pressure to round against or escape epithelial confinement. *Nat. Commun.* 6:8872. https://doi.org/10.1038/ncomms9872

Stewart, M.P., J. Helenius, Y. Toyoda, S.P. Ramanathan, D.J. Muller, and A.A. Hyman. 2011. Hydrostatic pressure and the actomyosin cortex drive mitotic cell rounding. *Nature.* 469:226–230. https://doi.org/10.1038/nature09642

Straight, A.F., A. Cheung, J. Limouze, I. Chen, N.J. Westwood, J.R. Sellers, and T.J. Mitchison. 2003. Dissecting temporal and spatial control of cytokinesis with a myosin II inhibitor. *Science.* 299:1743–1747. https://doi.org/10.1126/science.1081412

Takigawa, T., Y. Morino, K. Urayama, and T. Masuda. 1996. Poisson's ratio of polyacrylamide (PAAm) gels. *Polymer Gels and Networks.* 4:1–5. https://doi.org/10.1016/0966-7822(95)00013-5

Tambe, D.T., C.C. Hardin, T.E. Angelini, K. Rajendran, C.Y. Park, X. Serra-Picamal, E.H. Zhou, M.H. Zaman, J.P. Butler, D.A. Weitz, et al. 2011. Collective cell guidance by cooperative intercellular forces. *Nat. Mater.* 10:469–475. https://doi.org/10.1038/nmat3025

Thielicke, W., and E.J. Stamhuis. 2014. PIVlab – towards user-friendly, affordable and accurate digital particle image velocimetry in MATLAB. *Journal of Open Research Softwware.* 2:e30. https://doi.org/10.5334/jors.bl

Towns, J., T. Cockerill, M. Dahan, I. Foster, K. Gaither, A. Grimshaw, V. Hazlewood, S. Lathrop, D. Lifka, G.D. Peterson, et al. 2014. XSEDE: Accelerating Scientific Discovery. *Comput. Sci. Eng.* 16:62–74. https://doi.org/10.1109/MCSE.2014.80

Trepat, X., M.R. Wasserman, T.E. Angelini, E. Millet, D.A. Weitz, J.P. Butler, and J.J. Fredberg. 2009. Physical forces during collective cell migration. *Nature Physics.* 5:426–430. https://doi.org/10.1038/nphys1269

Trickey, W.R., F.P.T. Baaijens, T.A. Laursen, L.G. Alexopoulos, and F. Guilak. 2006. Determination of the Poisson's ratio of the cell: recovery properties of chondrocytes after release from complete micropipette aspiration. *J. Biomech.* 39:78–87. https://doi.org/10.1016/j.jbiomech.2004.11.006

Troxell, M.L., S. Gopalakrishnan, J. McCormack, B.A. Poteat, J. Pennington, S.M. Garringer, E.E. Schneeberger, W.J. Nelson, and J.A. Marrs. 2000. Inhibiting cadherin function by dominant mutant E-cadherin expression increases the extent of tight junction assembly. *J. Cell Sci.* 113: 985–996. https://doi.org/10.1242/jcs.113.6.985

Tse, J.R., and A.J. Engler. 2010. Preparation of hydrogel substrates with tunable mechanical properties. *Curr. Protoc. Cell Biol.* Chapter 10:16. https://doi.org/10.1002/0471143030.cb1016s47

Underhill, P.T., and P.S. Doyle. 2004. On the coarse-graining of polymers into bead-spring chains. *Journal of Non-Newtonian Fluid Mechanics.* 122:3–31. https://doi.org/10.1016/j.jnnfm.2003.10.006

Uroz, M., S. Wistorf, X. Serra-Picamal, V. Conte, M. Sales-Pardo, P. Roca-Cusachs, R. Guimerà, and X. Trepat. 2018. Regulation of cell cycle progression by cell-cell and cell–matrix forces. *Nat. Cell Biol.* 20: 646–654. https://doi.org/10.1038/s41556-018-0107-2
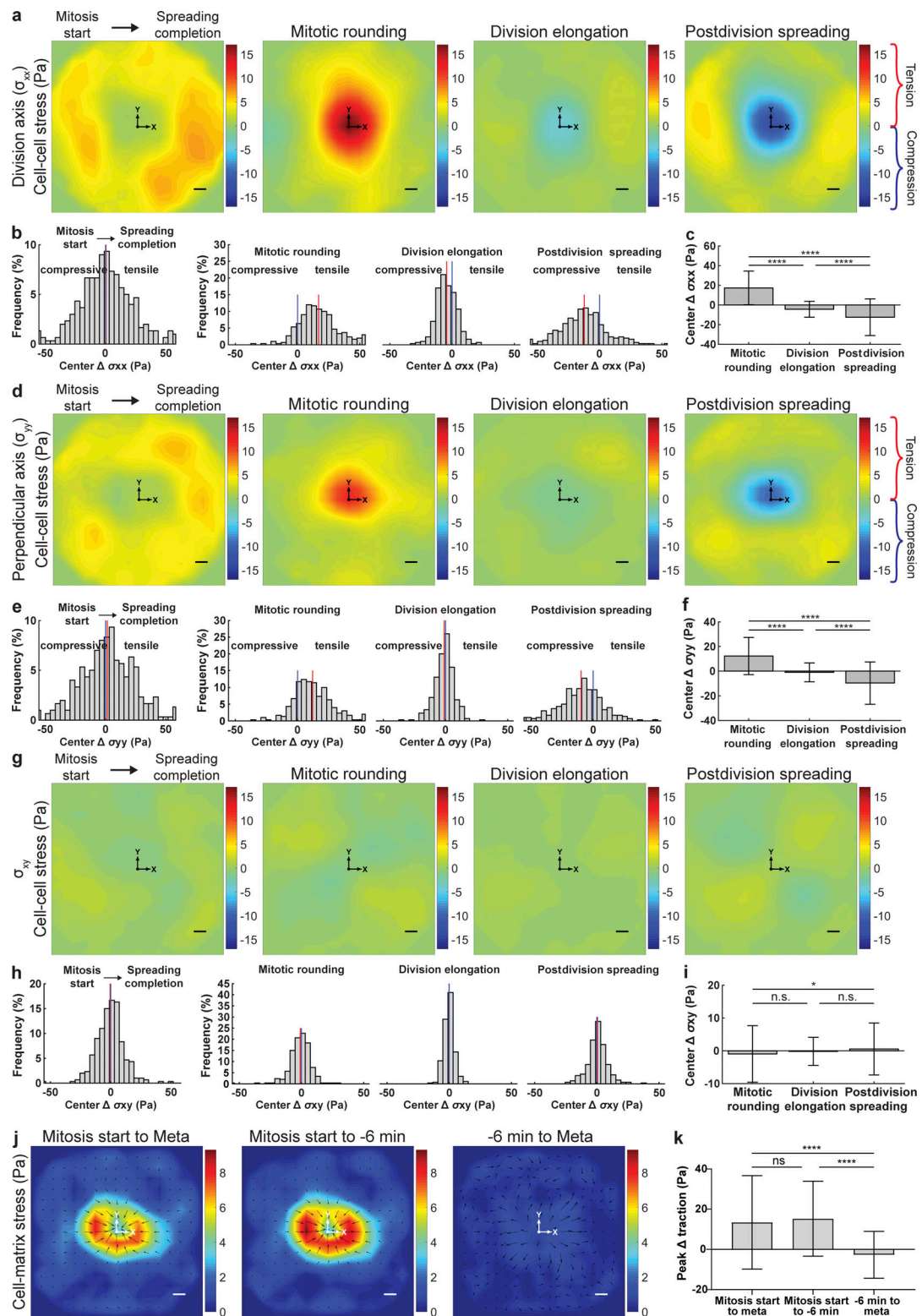
Supplemental material

Figure S1. **MDCK epithelial cell division is accompanied by distinct stages of cell–cell stress. (a–i)** Change in cell–cell stress along division axis (a–c), perpendicular axis (d–f), and shear directions (g–i) during division, represented as averaged heat maps (a, d, and g), distributions (b, e, and h), and average-value comparisons (c, f, and i) for entire division process (mitosis start to postdivision spreading completion), mitotic rounding, division elongation, and postdivision spreading. For heat maps, dividing cell is centered on the heat map, with the division axis oriented along the horizontal (x) axis. Mitotic rounding consists of inward and outward force generation stages. **(j and k)** Average change in cell–matrix stress during the course of mitotic rounding (from mitosis start to metaphase) from mitosis start to 6 min before metaphase, and from 6 min before metaphase to metaphase (j) and corresponding quantification (k). $n = 300$; ± SD for comparison bar graphs; for histograms, blue line indicates 0 Pa stress value, red line indicates mean; for comparisons, Tukey's multiple comparison test. Scale bars, 10 μm. *, $P < 0.05$; ****, $P < 0.0001$.
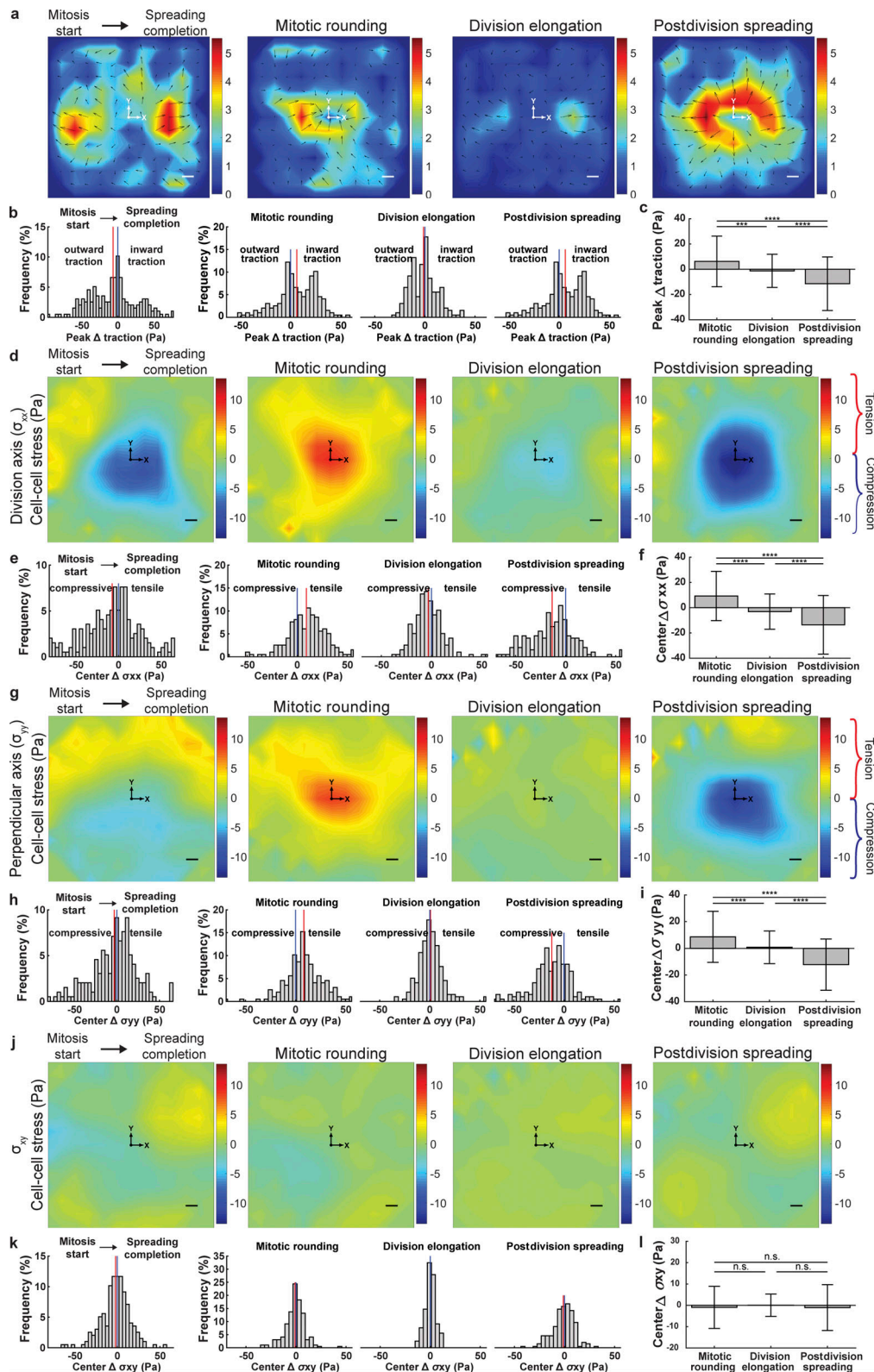
Figure S2. **MCF10A epithelial cell division is accompanied by distinct stages of cell–matrix and cell–cell stress. (a–l)** Change in cell–matrix stress (a–c) and cell–cell stress during division along division axis (d–f), perpendicular axis (g–i), and shear directions (j–l) represented as averaged heat maps (a, d, g, and j), distributions (b, e, h, and k), and average-value comparisons (c, f, i, and l) for entire division process (mitosis start to postdivision spreading completion), mitotic rounding, division elongation, and postdivision spreading. For heat maps, dividing cell is centered on the heat map, with the division axis oriented along the horizontal (x) axis. Outward (pointing away from the origin) traction stresses were defined to be negative, and inward (pointing toward the origin) traction stresses were defined to be positive. $n = 300$; ±SD for comparison bar graphs; for histograms, blue line indicates 0 Pa stress value, red line indicates mean; for comparisons, Tukey's multiple comparison test. Scale bars, 10 μm. ***, $P < 0.001$; ****, $P < 0.0001$.
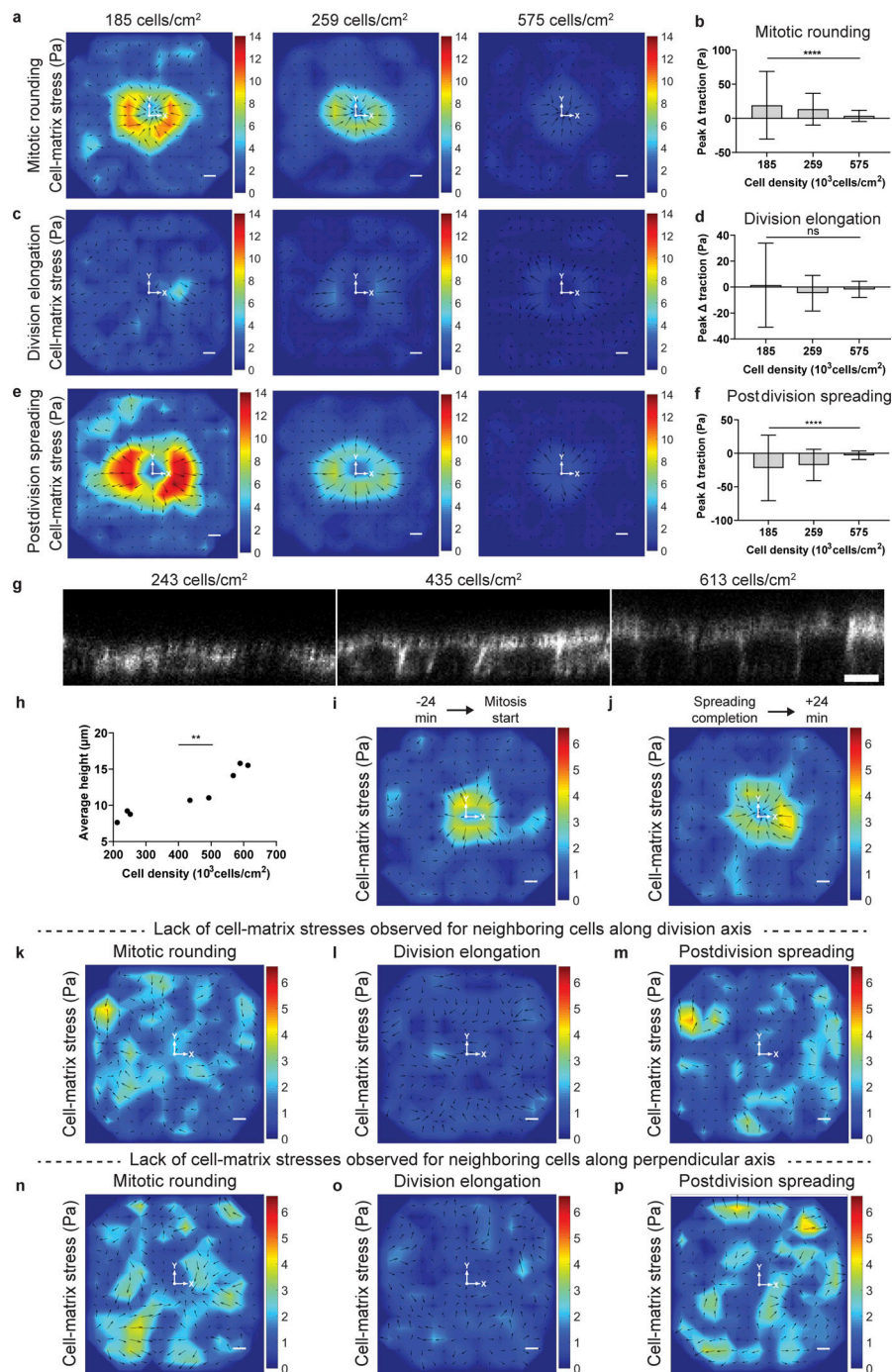
Figure S3. **Increasing epithelial monolayer densities are correlated with reduced measured division forces and increasing heights, and observed cell–matrix stresses are specific for dividing cells undergoing mitotic rounding, division elongation, and postdivision spreading. (a–f)** Change in cell–matrix stress during division at varying MDCK monolayer densities represented as averaged heat maps (a, c, and e) and average-value comparisons (b, d, and f), respectively, for mitotic rounding (a and b), division elongation (c and d), and postdivision spreading (e and f). For heat maps, dividing cell is centered on the heat map, with the division axis oriented along the horizontal (x) axis. Outward (pointing away from the origin) traction stresses were defined to be negative, and inward (pointing toward the origin) traction stresses were defined to be positive. $n = 140$ (low density), $n = 300$ (medium density), $n = 168$ (high density); ±SD; one-way ANOVA post-test for trend. ****, $P < 0.0001$. **(g and h)** Representative side-view images of MDCK cells stably expressing LifeAct:RFP at varying densities (g) and their height quantification (h). $n = 8$; Spearman's rank. **, $P < 0.01$. The increased cell heights and reduced cross-sectional areas at greater monolayer densities make the plane stress assumption used in MSM less valid, which could explain why measured cell division stresses decrease at increasing monolayer densities (Tambe et al., 2011). **(i and j)** Average change in cell–matrix stress before mitotic rounding (24 min before mitosis start to mitosis start, $n = 277$; i) and after postdivision spreading (postdivision spreading completion to 24 min later, $n = 300$; j). **(k–p)** Neighboring cells along the division axis or perpendicular axis do not exhibit distinct cell–matrix stresses while the dividing cell undergoes mitotic rounding, division elongation, or postdivision spreading. Average change in cell–matrix stress for neighboring cells along division axis (k–m) and perpendicular axis (n–p), while the dividing cell undergoes mitotic rounding (k and n), division elongation (l and o), and postdivision spreading (m and p). Neighboring cells are centered on the heat maps. $n = 78$. Scale bars, 10 µm.
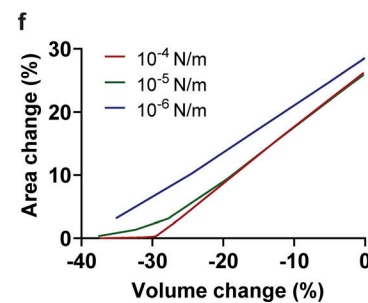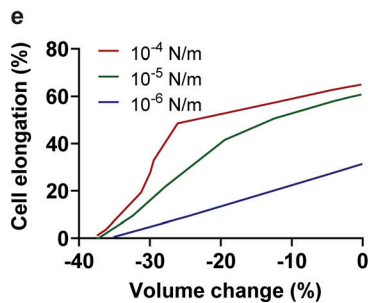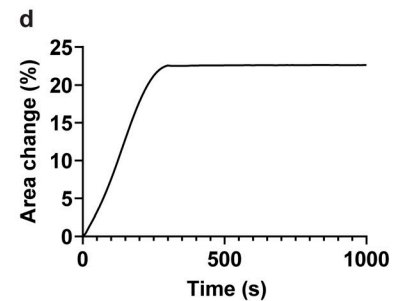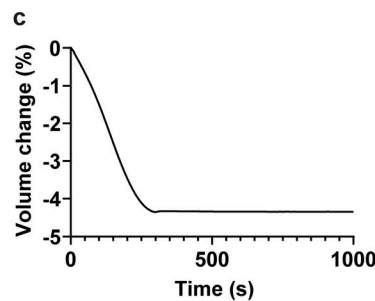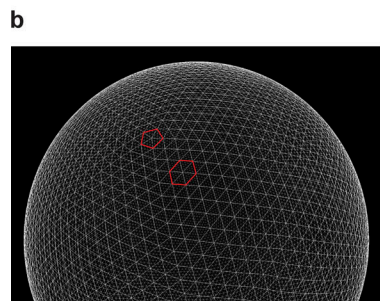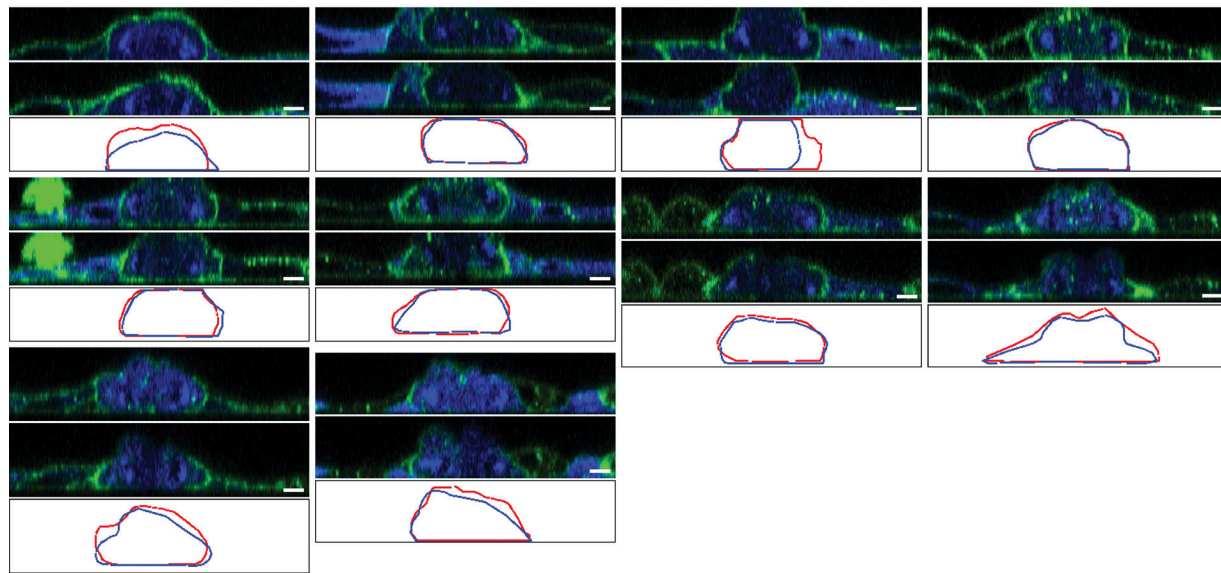
Figure S4. **The interpolar spindle does not bear compressive forces during division elongation, while varying levels of volume and area conservation during cytokinesis lead to cell elongation. (a)** Array of side-view images of MDCK cells before and after ablation, showing that 3D ablation of the interpolar spindle does not result in consistent retraction of the dividing cell. Scale bars, 5 µm. **(b)** A snapshot depicting coarse-grained triangular mesh consisting of pentagons and hexagons. **(c and d)** Volume change (c) and area change (d) during the progression of cytokinetic ring contraction corresponding to the case shown in Fig. 7 (b–d). **(e and f)** Final cell elongation vs final volume change (e), and final area change vs. final volume change (f) for varying degrees of area conservation.
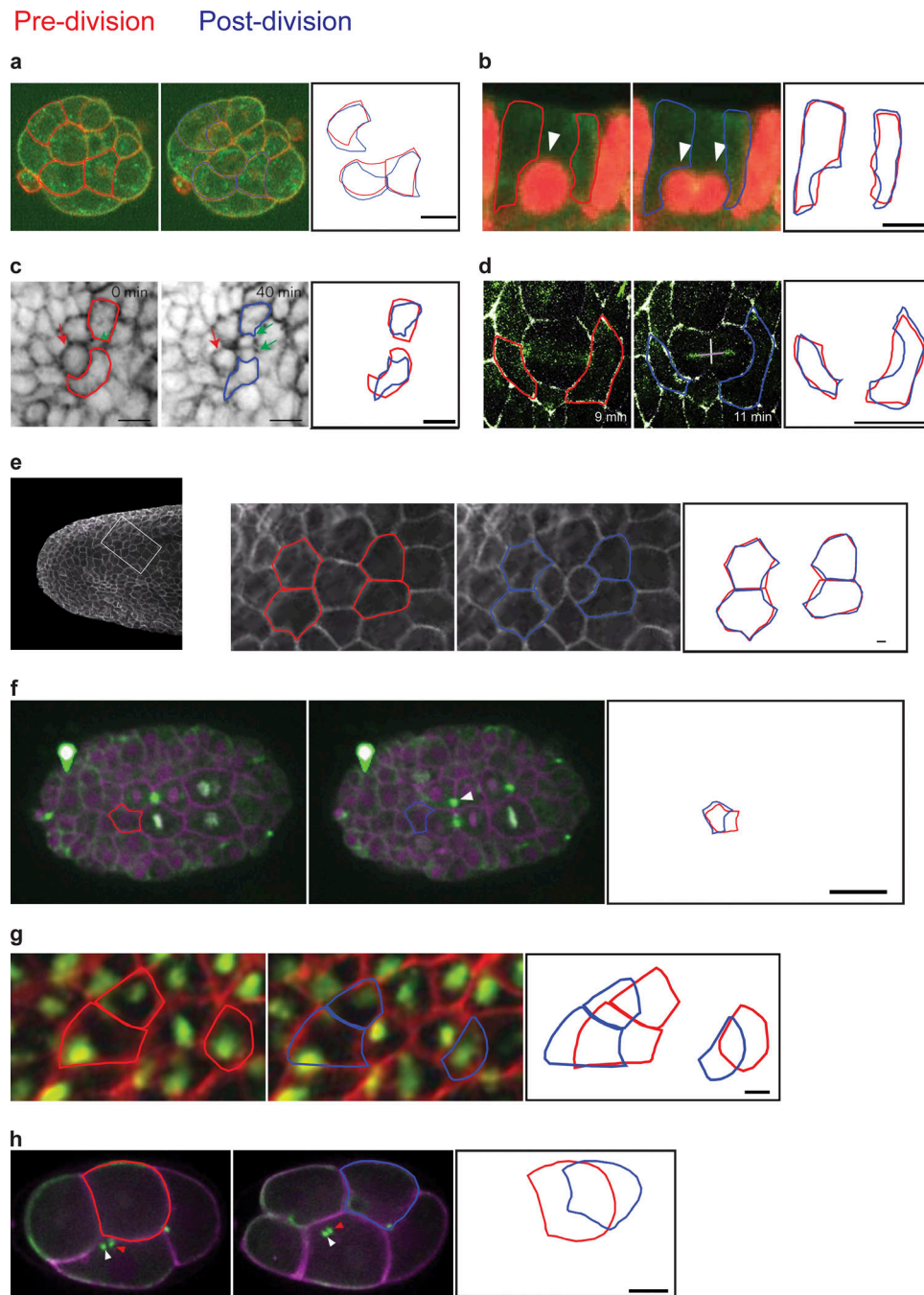
Figure S5.   **The forces of division elongation are universal across epithelia in vivo. (a–h)** Images of adjacent cell deformation during division within mouse blastocyst (E3; a), adult mouse intestinal organoid (b), embryonic (E15.5) mouse epidermis (c), *Drosophila* embryo segmentation (d), zebrafish larva epidermis (e), *C. elegans* embryo E8-16 (f), *Xenopus* embryo (g), and *C. elegans* embryo E5 (h). Scale bars, 15 µm (c), 10 µm (a, b, and d–h).

Table S1 and Table S2 are provided online. Table S1 lists information on replicates, number of data points, and statistical testing for all data shown. Table S2 lists the parameters employed in the computational model of cell elongation during cytokinesis due to varying levels of volume and area conservation.